The developing juvenile talus

Reid, Rebecca A. G.; Davies, Catriona; Cunningham, Craig

Published in:
Journal of Anatomy

DOI:
10.1111/joa.13940

Publication date:
2023

Received: 24 February 2023 | Revised: 20 June 2023 | Accepted: 19 July 2023

DOI: 10.1111/joa.13940

Journal of Anatomy ANATOMICAL SOCIETY WILEY

ORIGINAL ARTICLE

The developing juvenile talus: Radiographic identification of distinct ontogenetic phases and structural trajectories

Rebecca A. G. Reid | Catriona Davies | Craig Cunningham

Centre for Anatomy and Human Identification, School of Science and Engineering, University of Dundee, Dundee, UK

Correspondence
Rebecca A. G. Reid, Centre for Anatomy and Human Identification, School of Science and Engineering, University of Dundee, Dundee DD1 5EH, UK.
Email: 110006554@dundee.ac.uk

Abstract

Trabecular bone architecture in the developing skeleton is a widely researched area of bone biomechanics; however, despite its significance in weight-bearing locomotion, the developing talus has received limited examination. This study investigates the talus with the purpose of identifying ontogenetic phases and developmental patterns that contribute to the growing understanding of the developing juvenile skeleton. Colour gradient mapping and radiographic absorptiometry were utilised to investigate 62 human tali from 38 individuals, ranging in age-at-death from 28 weeks intrauterine to 20 years of age. The perinatal talus exhibited a rudimentary pattern comparable to the structural organisation observed within the late adolescent talus. This early internal organisation is hypothesised to be related to the vascular pattern of the talus. After 2 years of age, the talus demonstrated refinement, where radiographic trajectories progressively developed into patterns consistent with adult trabecular organisation, which are linked to the forces associated with the bipedal gait, suggesting a strong influence of biomechanical forces on the development of the talus.

KEYWORDS
biomechanics, bone, development, juvenile, radiography, talus, trabeculae

1 | INTRODUCTION

The influence of biomechanical factors upon the adult skeleton, in particular the trabecular bone, is well documented (Barak et al., 2011; Currey, 1984; Frost, 2003; Ruff et al., 2006; Ruimerman et al., 2005). However, the influence of changing biomechanical forces associated with the attainment of motor milestones and bipedal gait during juvenile development is not completely understood (Ryan et al., 2017; Saers et al., 2022). Trabecular development of the juvenile skeleton has been predominately studied within the long bones, including the femur (Djuric et al., 2012; Milovanovic et al., 2017; Modlesky et al., 2014; Osborne et al., 1980; Reissis & Abel, 2012; Ryan et al., 2017; Ryan & Krovitz, 2006; Salle et al., 2002), tibia (Burrows et al., 2010; Ding et al., 2012; Goliath et al., 2022; Gosman & Ketcham, 2009; Raichlen et al., 2015; Reid et al., 2023), humerus (Perchalski et al., 2018; Reissis & Abel, 2012; Ryan et al., 2017), and radius (Colombo et al., 2019). There are also a growing number of studies investigating irregular bones such as the ribs (Beresheim et al., 2020), vertebral column (Acquaah et al., 2015; Goodchild, 2019; Kneissel et al., 1997; Nuzzo et al., 2003; Roschger et al., 2001; Yusof, 2013), innominate (Abel & Macho, 2011; Cunningham & Black, 2009a, 2009b; Glorieux et al., 2000; Maclean, 2017; Maclean et al., 2014), scapula (O'Malley, 2013), and calcaneus (Saers et al., 2019).

The trabecular development of the juvenile human talus, however, has received limited investigation except for Figus, Stephens, Sorrentino, Bortolini, Arrighi, Higgins, et al. (2022) and Figus,

Stephens, Sorrentino, Bortolini, Arrighi, Lugli, et al. (2022). Figus, Stephens, Sorrentino, Bortolini, Arrighi, Higgins, et al. (2022) examined the talus from 36 weeks intrauterine to 2 postnatal years, while Figus, Stephens, Sorrentino, Bortolini, Arrighi, Lugli, et al. (2022) investigated the talus from 8 postnatal weeks to 10 years of age through geometric morphometric and whole-bone trabecular analysis. In a Late Roman to 20th century sample, Figus, Stephens, Sorrentino, Bortolini, Arrighi, Higgins, et al. (2022) compared pre-loading specimens ($n = 11$, <6 postnatal months) with post-loading specimens ($n = 17$, 6–24 postnatal months). The pre-loading talus had an isotropic structure with densely packed trabeculae and a high bone volume fraction on the medial side of the talus and head. After loading, bone volume fraction and trabecular number decreased while trabecular thickness, separation, and anisotropy increased, suggesting the acquisition of the bipedal gait influences the internal structure of the talus. Figus, Stephens, Sorrentino, Bortolini, Arrighi, Lugli, et al. (2022) continued this work and demonstrated that anisotropy and bone volume fraction become more heterogeneous after loading. This current work aims to add to the growing understanding of the developing juvenile talus by radiographically identifying ontogenetic phases and developmental patterns in the talus from 28 weeks intrauterine to 20 years of age. This will provide a general overview of the internal changes and a detailed descriptive synopsis of the internal arrangement of the talus during each ontogenetic phase. The impact of different factors, such as changing biomechanical loads and vascularisation, upon these internal changes will be considered to better understand the development of the talus over a wide age range.

Analysis of the developing talus may have important clinical applications in the treatment of paediatric trauma and the therapeutic intervention of some pathological conditions, such as juvenile idiopathic arthritis and talipes equinovarus. The talus has an important role in locomotion and weight-bearing within the talocrural joint (Soames & Palastanga, 2019). Bodyweight is transmitted down through the vertebral column and pelvis, through the lower limbs, and into the foot via the ankle joint during the bipedal gait and passive standing (Soames & Palastanga, 2019). The trabecular architecture of the adult talus facilitates the dispersion of these stresses, in addition to ground reaction forces (Pal & Routal, 1998).

The trabecular architecture of the adult talus has been extensively examined, with several studies subdividing their analyses into the talar head, neck, and body (Athavale et al., 2008; Ebraheim et al., 1999; Pal & Routal, 1998; Takechi et al., 1982). While some disagreements exist regarding the exact internal structure of the talar body, there is a consensus that the trabeculae within the body transmit forces both anteriorly through the navicular, towards the metatarsals, and inferiorly towards the calcaneus (Athavale et al., 2008; Ebraheim et al., 1999; Pal & Routal, 1998; Takechi et al., 1982). The conflict within the literature regarding the organisation of the adult body of the talus pertains to the organisation of the trabeculae. Ebraheim et al. (1999) and Pal and Routal (1998) both identified parallel trabecular plates running in the sagittal plane within the body, while Athavale et al. (2008) and Takechi et al. (1982) describe that the talar body trabeculae are orientated in two directions. Su et al. (2013) identified trabeculae within the anteromedial and anterocentral portions of the body, extending in an anteroinferior direction parallel with the talar neck. Additionally, Su et al. (2013) described the trabeculae in the posterolateral trochlea as orientated slightly posteriorly towards the calcaneus, which agrees with the structure described by Athavale et al. (2008) and Takechi et al. (1982). Furthermore, the lateral portion of the trochlea appears to be an area of high trabecular bone volume fraction (BV/TV), the ratio of trabecular bone to total volume within a volume of interest (Saers et al., 2018; Tsegai et al., 2017). This appears similar to the distribution of contact pressure modelled by Bae et al. (2015) on the trochlear surface, with areas of high pressure occurring during the midstance and push-off phases of the gait cycle appearing on the antero-lateral quadrant of the talar surface, suggesting this area is adapted to facilitate high pressures (Bae et al., 2015).

Meanwhile, the neck of the adult talus is described as a dense, irregular network of trabeculae (Ebraheim et al., 1999; Pal & Routal, 1998; Sinha, 1985; Takechi et al., 1982). However, Athavale et al. (2008) and Su et al. (2013) disagree with this and describe the talar neck as organised and a continuation of the plates observed within the talar body. The trabecular architecture of the neck of the talus appears to facilitate the transmission of forces both anteriorly towards the forefoot and inferiorly towards the calcaneus (Pal & Routal, 1998). The talar head exhibits curved plates of trabeculae along the sagittal plane with high BV/TV at the articular surface for the navicular (Athavale et al., 2008; Ebraheim et al., 1999; Krause et al., 2013; Pal & Routal, 1998; Saers et al., 2018; Sinha, 1985; Takechi et al., 1982; Tsegai et al., 2017). This trabecular arrangement is likely to facilitate the transmission of compressive forces to the metatarsals, as demonstrated via finite element analysis (Gefen et al., 2000).

The adult body of the talus appears to be highly variable between individuals (Tsegai et al., 2017). Loading patterns are reflected in the trabecular architecture of the talus (Hébert et al., 2012; Saers et al., 2018; Su et al., 2013; Tsegai et al., 2017). This has been demonstrated in comparative studies between humans and primates with different locomotive strategies (Hébert et al., 2012; Su et al., 2013; Tsegai et al., 2017) and in humans with varying mobility levels (Saers et al., 2018). Therefore, the body of the talus presents an area of the developing skeleton that may be sensitive to biomechanical changes occurring during ontogeny when an infant learns to sit upright, crawl, and walk. The results of Figus, Stephens, Sorrentino, Bortolini, Arrighi, Higgins, et al. (2022) and Figus, Stephens, Sorrentino, Bortolini, Arrighi, Lugli, et al., 2022) indicate that the talus is influenced by these biomechanical changes. This work seeks to confirm this radiographically over a wider age range.

There are several motor milestones to be achieved during the development of locomotion that result in changing biomechanical loads on the talus (Keen, 1993). Biomechanical influences are present intrauterine. Muscle development occurs at approximately 7 weeks of gestation, with spontaneous muscle contractions appearing at 9 weeks (Rose & Gamble, 1994). Typically, intrauterine movements arise at 15 weeks, with the level of activity increasing significantly in the latter half of the gestational period (de Vries et al., 1982; Verbruggen et al., 2018).

This intrauterine loading includes movement of the foetus against the uterus wall, resistance of movement by the amniotic fluid, and loading specific to muscle movements of the foetus (Rose & Gamble, 1994). Early new-born stepping can occur from 32 weeks of gestation and persist until 2 months postnatal, which consists of alternating flexion and extension of the legs while held in an upright position (Okamoto et al., 2003; Rose & Gamble, 1994).

The ability to sit upright is achieved at 6–7 months (Keen, 1993). The onset of crawling occurs at approximately 4–9 months (Adolph et al., 1998). In a longitudinal study of 28 infants, the majority of infants displayed typical postural changes expected during crawling; however, some omitted specific crawling stages or had a blend of stages rather than distinct crawling stages, demonstrating the variability of crawling between individuals (Adolph et al., 1998). Typically, the onset of walking occurs at approximately 12–14.5 months of age (Keen, 1993; Størvold et al., 2013). Rose and Gamble (1994) noted that individuals have their own idiosyncratic method of walking, as the attainment of the bipedal gait is a learned ability that often demonstrates variability between individuals.

Early walking is typically described as having a wide stance (Cowgill et al., 2010; Hallemans et al., 2005; Johnston et al., 2014; Sutherland, 1997; Sutherland et al., 1988), simultaneous flexion of the knee and hip (Cowgill et al., 2010; Hallemans et al., 2005), and an initial ground contact of the foot that varies from either heel–toe, whole foot, or toe–heel (Johnston et al., 2014). However, several studies state that there is an absence of heel strike during early walking (Hallemans et al., 2005; Sutherland et al., 1988), with the ankle in neutral dorsiflexion (Rose & Gamble, 1994). During this stage, gait has a low average speed, a high cadence, short step length, and prolonged double limb support (Hallemans et al., 2005). Several studies examining the development of unassisted walking note that the initial gait pattern is extremely irregular and associated with variable walking strategies, stride lengths and widths, and foot rotation (Adolph et al., 2003; Bisi & Stagni, 2015). Muscle activity of the lower limbs is also highly variable during early walking (Chang et al., 2006), with gross activation of muscles and a lack of a standard pattern of muscle activity (Okamoto et al., 2003).

The development of the longitudinal arch of the foot is linked to the maturation of the bipedal gait. During early walking, the plantar fat pad defends the foot against overloading, dispersing the plantar pressure throughout the foot (Bosch et al., 2007). As a result, peak plantar pressures within the midfoot are greater in infants in comparison to adults (Hallemans et al., 2003). After 18 months of age, there is a shift in load from the midfoot to the heel and forefoot as the longitudinal arch of the foot develops (Bertsch et al., 2004; Bosch et al., 2007). At this stage, heel strike evolves, with ankle plantarflexion during gait developing (Bertsch et al., 2004; Sutherland et al., 1988).

With experience, the bipedal gait becomes more standardised, which has been observed beginning 2 months after the onset of unassisted walking (Bisi & Stagni, 2015). With age, step length and width increase (Bisi & Stagni, 2015; Cowgill et al., 2010), walking speed increases, a normal arm swing appears (Cowgill et al., 2010), and foot rotation decreases (Bisi & Stagni, 2015). There is debate within the literature regarding the timing of maturation of the bipedal gait; however, it appears to occur between 4 and 8 years of age (Saers et al., 2019; Sutherland, 1997).

Evidence for the relationship between locomotive development and trabecular change is demonstrated by the substantial shift in trabecular development associated with a decrease in BV/TV between 6 and 12 months, coinciding with the onset of walking (Acquaah et al., 2015; Figus, Stephens, Sorrentino, Bortolini, Arrighi, Higgins, et al., 2022; Figus, Stephens, Sorrentino, Bortolini, Arrighi, Lugli, et al., 2022; Gosman & Ketcham, 2009; Milovanovic et al., 2017; Ryan et al., 2017; Ryan & Krovitz, 2006; Saers et al., 2019), and this phenomenon occurring earlier within the distal radius, indicating the influence of crawling (Colombo et al., 2019). The biomechanical influence upon the skeleton is also demonstrated by the structural heterogeneity within bones designed to withstand specific locomotive forces (Acquaah et al., 2015; Figus, Stephens, Sorrentino, Bortolini, Arrighi, Lugli, et al., 2022; Gosman & Ketcham, 2009; Milovanovic et al., 2017; Ryan & Krovitz, 2006; Saers et al., 2019). Additionally, differential developmental rates exist within the skeleton, which appear to be increased in bones required to accommodate bipedal forces (Ryan et al., 2017). Finally, the achievement of adult-like organisation around 8 years of age, coinciding with the maturation of the bipedal gait (Ding et al., 2012; Gosman & Ketcham, 2009; Saers et al., 2019), is also indicative of a strong biomechanical influence upon skeletal development. Reid et al. (2023) discuss these adaptions in further detail.

Patterns of adult trabecular organisation have been observed in the prenatal scapula, ilium, and sacrum (Abel & Macho, 2011; Cunningham & Black, 2009a, 2009b; O'Malley, 2013; Yusof, 2013). For example, in both a radiographic and computed tomography study, Cunningham and Black (2009a, 2009b) observed a distinctive pattern in the foetal and neonatal ilium, with dense bone corresponding to the acetabulum, trabecular chiasma, and sciatic notch. This pattern was also observed within the adult ilium and has been attributed to the dispersion of loads for bipedal locomotion (Cunningham & Black, 2009a, 2009b). Abel and Macho (2011) also observed the sacro-pubic bundle and ischio-iliac strut in young individuals, thereby agreeing with Cunningham and Black (2009a, 2009b) that the ilium has an early internal organisation similar to the adult form. However, this has not been witnessed within long bones (Gosman & Ketcham, 2009; Raichlen et al., 2015; Reid et al., 2023; Ryan & Krovitz, 2006). The reason why adult trabecular organisation exists in some areas of the juvenile skeleton is unknown; however, intrauterine movements, vascularisation, and/or a pre-determined genetic template of trabecular structure have been suggested (Cunningham & Black, 2009a, 2009b, 2013).

The ossification pattern also appears to have an influence on trabecular development. Saers et al. (2019) proposed that the ossification pattern in the calcaneus results in differences in its trabecular development in comparison to long bones. In particular, this involved the increase in degree of anisotropy (DA), the extent to which trabeculae are similarly aligned, during the first year of life in

contrast to the decrease in DA observed within long bones (Saers et al., 2019). Saers et al. (2019) observed that the trabeculae within the developing calcaneus were dense and anisotropic, radiating from its ossification centre. In comparison, long bones ossify in one direction rather than radiating in several directions; therefore, this is suggested to influence the trabecular organisation (Saers et al., 2019). This appears to also impact the development of the talus, with DA increasing after 6 post-natal months (Figus, Stephens, Sorrentino, Bortolini, Arrighi, Higgins, et al., 2022).

Ossification of the talus occurs typically around 6 months of gestation (Agrawal et al., 1984; Baker et al., 2005; Cheng et al., 1995, 1997; Cunningham et al., 2016; Czerwiński et al., 2001; Gardner et al., 1959; Hubbard et al., 1993). The ossification centre may originate from more than one nucleus but will rapidly form a single ossification centre (Cunningham et al., 2016). The primary ossification centre of the talus is initially located in the neck region of the bone, being described as either within the central neck (Fritsch et al., 1996; Hubbard et al., 1993), the inferior neck (Cheng et al., 1997), or in the neck anterior to the trochlear articular facets (Agrawal et al., 1984). Ossification continues from the primary ossification centre, expanding distally, proximally, and medially (Hubbard et al., 1993). At 3 months postnatal, 55% of the talus is reported to be ossified (Hubbard et al., 1993). As a result, during the perinatal period, the talus appears small and ovoid in shape, compressed superior-inferiorly (Baker et al., 2005; Cunningham et al., 2016). The talus gradually becomes more recognisable as development proceeds, with the lateral process and tarsal sinus ossifying postnatally at approximately 5 months, and by 7 months, the neck of the talus becomes defined (Cunningham et al., 2016). By 2 years of age, the talus has a recognisable adult morphology (Baker et al., 2005). The articular facets of the talus develop clear boundaries by 6 years of age (Cunningham et al., 2016). The posterior tubercle of the talus ossifies later in childhood in females between 7 and 8 years and between 9 and 10 years in males (Cunningham et al., 2016).

Vascularisation of bone also appears to impact the organisation of trabeculae (Cunningham & Black, 2010, 2013). In an investigation of the neonatal ilium, a vascular collar of cortical bone extending into the trabecular space was observed, originating from the nutrient foramen. Thickened trabeculae were observed surrounding this collar. The nutrient foramen provides blood to the bone via the nutrient artery, and its invasion triggers endochondral ossification. As a result, the presence of the nutrient artery precedes the formation of trabeculae, which must therefore grow around the vessels, which thus influences the trabecular architecture (Cunningham & Black, 2013). This pattern of thickened trabeculae around vasculature has also been observed in the scapula and ischium (Maclean et al., 2014; O'Malley, 2013). The talus demonstrates a complex vascular pattern that may influence the development of its internal structures (Figure 1). The cartilage model of the talus is the first of the tarsals to experience vascular invasion (Cheng et al., 1997; Fritsch et al., 1996), with cartilage canals appearing between 9 and 12 weeks (Agrawal et al., 1984; Gardner et al., 1959). By the perinatal period, the talus is supplied by vessels from branches of the sinus tarsi, deltoid, and superior neck vessels (Fritsch et al., 1996).

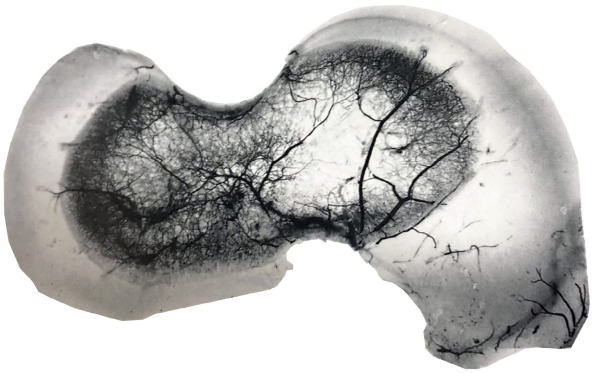

FIGURE 1 Sagittal section of the talus at 2.5 years with an arterial injection. From An Atlas of Vascular Anatomy of the Skeleton and Spinal Cord, Edn. 1 by Crock (1996). Reproduced by permission of Taylor & Francis Group.

The existing research literature continues to enhance knowledge and understanding of juvenile skeletal development; nevertheless, gaps in our knowledge still exist. The talus presents an irregular bone, which deviates from the developmental studies that have predominantly focused on the long bones. Thus, a radiographic investigation of the talus aims to contribute to the growing understanding of juvenile skeletal ontogeny by providing a detailed description of the changes to the internal organisation of the talus and identifying ontogenetic phases and developmental patterns, over an expanded age range in comparison to previous studies.

2 | MATERIALS AND METHODS

2.1 | Sample selection

Sixty-two human tali from 38 individuals were available for examination from the Scheuer Collection within the Centre for Anatomy and Human Identification, University of Dundee. The Scheuer Collection is an active juvenile skeletal repository from European archaeological and historical anatomical sources. Documented information was available for 11 individuals, with age-at-death being estimated for most of the sample. Three historical anatomical specimens were included in this study, with the remainder being archaeological. Ethical approval is in place for research upon this skeletal collection from the HM Inspector for Anatomy, Scotland. Specimens were selected based on the following criteria: no extensive post-mortem damage, pathology, or soft tissue, nor articulated with other skeletal elements. The specimens included with post-mortem damage exhibited cortical erosion, and if damage to the trabecular bone was present, it was deemed minimal. Specimens included in the analysis ranged in age from 28 weeks intrauterine to 20 years (Table 1). Definitions of early and

TABLE 1 Sample composition.

Age		Number of specimens	Number of individuals	Left	Right
Foetal	28–38 weeks	4	3	1	3
Perinatal	Term	10	7	4	6
Infancy	0–≤12 months	2	2	1	1
Early childhood	>1–≤8 years	19	11	9	10
Late childhood	>8–20 years	27	15	13	14
Total		62	38	28	34

late childhood are adapted from Ryan et al. (2017), who divided childhood into early (1–5 years), middle (5–10 years), and late (10–18 years). In this study, childhood was subdivided into two periods before and after 8 years of age due to the observations throughout the literature that typically, adult trabecular quantity and structure are achieved at 8 years of age, as observed in the tibia (Gosman & Ketcham, 2009), calcaneus (Saers et al., 2019), and vertebrae (Roschger et al., 2001).

2.2 | Radiography and colour mapping

The radiographic protocol combining colour gradient maps with radiographic absorptiometry outlined in Reid et al. (2023) was adopted. This method uses an aluminium step wedge to calibrate levels of x-ray absorption and to provide a standard reference for comparison between smaller and larger specimens. The grey levels of each step of the step wedge were measured in Adobe Photoshop 2021 version 22.3.1. A calibration plot for each radiograph was produced for grey level versus aluminium bone mineral density equivalents (Al BMDE), where Al BMDE equals the known step thickness multiplied by step wedge density. The radiographic JPG images were converted into colour gradient maps using Adobe Photoshop 2021 version 22.3.1 using standardised settings. The grey level versus AL BMDE calibration plot was then used to calculate the Al BMDE for each colour on the colour map. The resultant colour gradient maps correlate Al BMDE to four different colours (yellow, violet, orange, and blue) and provide an AL BMDE scale bar for reference. Areas of violet depict low Al BMDE values; orange depicts medium Al BMDE values; and blue indicates high Al BMDE values.

The inferior and lateral views of the talus were radiographed within the Centre for Anatomy and Human Identification, University of Dundee, using a Saxo Mobile X-ray Unit. All specimens were placed upon 1.5 cm thick Oasis Ideal Max Life Wet Floral foam, with parafilm stretched over the foam surface to prevent any foam particles from entering bone with cortical erosion or via the vascular foramina. The inferior view was accomplished by placing the plantar surface of the talus upon the foam, while the lateral view was achieved by gently pressing the lateral process of the talus into the foam. In specimens where the lateral process had not developed, the lateral side of the talus was gently pressed into the foam to stabilise it. Exposure settings of 55 kV and 1.6 mA with a focal distance of 100 cm were utilised throughout the radiographic study.

2.3 | Developmental analysis

The colour maps for all individuals were placed in groups of shared morphology and radiographic patterns without any knowledge of the age-at-death of the specimens. More specifically, group 1 specimens were comprised of tali that were spherical, while group 2 tali had a "peanut-like" morphology. In Groups 3 and 4, the talus had a recognisable head, neck, and body, and the two groups were distinguished from each other by their radiodensities. Specimens within Group 5 had developed their lateral process, as did specimens from Group 6, but this latter group also had an elongation of the neck. Group 7 specimens shared a morphology with Group 6 but had a distinct radiographic pattern.

Age-at-death information was added to each group once all the colour maps had been assigned to a group. Areas of violet were interpreted as areas of low Al BMDE values, orange as medium Al BMDE values, and blue as areas of high Al BMDE values. Bilateral asymmetry was assessed by comparing whether each talus had been assigned to the same developmental group as its antimere. An exact sign test was used to assess whether group differences existed between observations of antimeres ($\alpha = 0.05$).

2.4 | Intra-observer agreement

To assess intra-observer agreement, the assignment of each colour map to a development group was repeated without knowledge of which individual each specimen belonged to or age-at-death. The developmental group assigned was compared to the original assessment using a weighted kappa analysis with linear weights (Cicchetti & Allison, 1971) to assess agreement. Statistical analysis was conducted using SPSS v28.

3 | RESULTS

An exact sign test was conducted to assess whether median group differences existed between observations of antimeres. Of the 21 pairs of tali, 3 individuals had tali that were assigned to different developmental groups. There was no statistically significant median difference in the assignment of antimeres to developmental groups ($p = 0.250$). Post-mortem damage was present on two of these

individuals, which may have influenced the assessment of the talus morphology.

Colour maps of the talus were divided into seven developmental groups based on a shared morphology and radiographic patterns (Table 2 and Figure 2).

To assess intra-observer agreement, the placement of colour maps of 62 specimens into developmental groups was repeated. There was a statistically significant agreement between the two analyses, $k_w = 0.977$ (95% CI, 0.958 to 0.995), $p < 0.0005$. The strength of agreement was classified as very good according to Landis and Koch (1977).

3.1 | Group 1 (28–38 weeks intrauterine)

Group 1 was limited to four foetal specimens from three individuals, which appeared both morphologically and radiographically distinct from the rest of the talar sample (Figure 3). Morphologically, the talus appeared as an osseous sphere ranging 4–8 mm in diameter. The lack of osteological features in the talus at this stage prevented orientation of the specimen. Therefore, only one radiographic view was conducted for these specimens. The small size of the specimens limited the radiological details. In specimens aged 28 weeks intrauterine, the talus appeared as a radiodense sphere lacking a shared pattern between specimens; however, by 38 weeks, the centre of the talus demonstrated greater AI BMDE than the periphery of the bone (Figure 4, arrows 1 and 2).

TABLE 2 Identified developmental groups.

Group	Number of specimens	Number of individuals	Age range
1	4	3	28–38 weeks intrauterine
2	11	8	Birth–6 months
3	1	1	1 year
4	12	8	2–8 years
5	9	5	5–9 years
6	13	7	9–14 years
7	11	6	16 years–20 years

3.2 | Group 2 (birth–6 months)

The 11 specimens, from 8 individuals, assigned to Group 2 were predominately perinatal specimens. At this stage, the tali appeared 'peanut-like' in morphology, with the sinus tarsi and neck becoming evident (Figures 5 and 6). The increase in size in comparison to Group 1 resulted in an increase in observable radiological features (Figure 3). Despite the specimens in this group ranging in radiodensity and radiolucency, a common pattern was observed within the specimens (Figures 3 and 4). The shared pattern within Group 2 consisted of a C-shaped radiodensity within the centre of the talus associated with elevated AI BMDE levels in comparison to the rest of the talus (Figure 6, arrows 1 and 2). When viewed radiographically from the lateral perspective, this area appeared to be located towards the plantar surface of the bone in the region of the developing sinus tarsi (Figure 6, arrows 3 and 4).

3.3 | Group 3 (1 year)

A single specimen with a recorded age-at-death of 1 year old was assigned to Group 3. This specimen demonstrated post-mortem damage with extensive cortical erosion and exposure of the underlying trabeculae; however, it was included in the sample due to a paucity of specimens of such age (Figure 7). Morphologically, the talus had developed in mass in comparison to Group 2, and the curvature of the lateral process was beginning to become evident

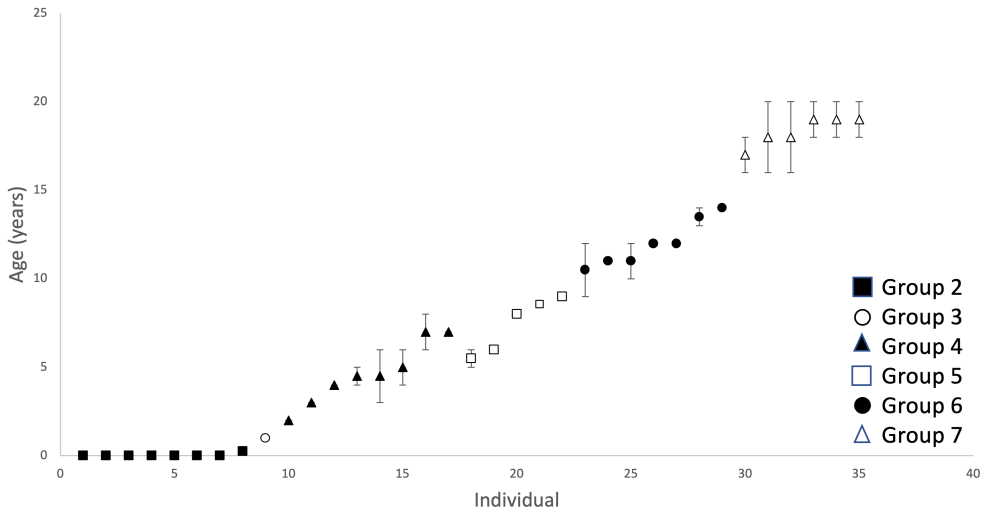

FIGURE 2 Age distribution of each developmental group, excluding Group 1. Error bars indicate an estimated age-at-death range. Perinatal individuals were assigned 0 years of age.

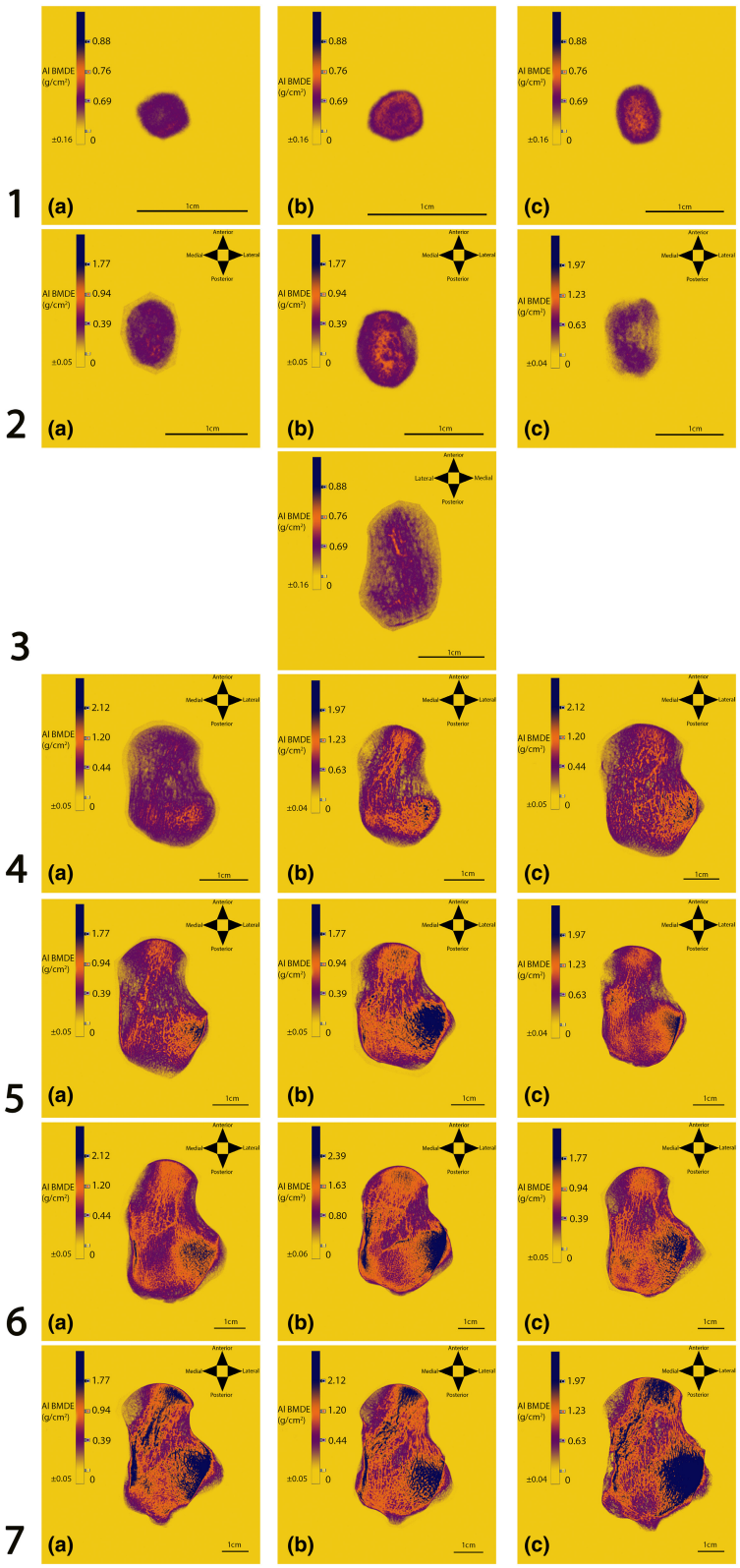

FIGURE 3 Inferior view of the developing talus (with the exception of the non-orientated Group 1). Group assignment on the left side of the figure. (a) Least developed; (b) median development; (c) most developed specimen within each developmental group. AI BMDE scale in each image.

(Figure 3). From the inferior view, the body of the talus had a trajectory running from the medial body to the antero-lateral head that appeared to have elevated AI BMDE in comparison to the remainder of the talus (Figure 7, arrows 1 and 3). The lateral body also appears to have medium AI BMDE (Figure 7, arrow 2). From the lateral view, the body of the talus also appeared radiodense, with

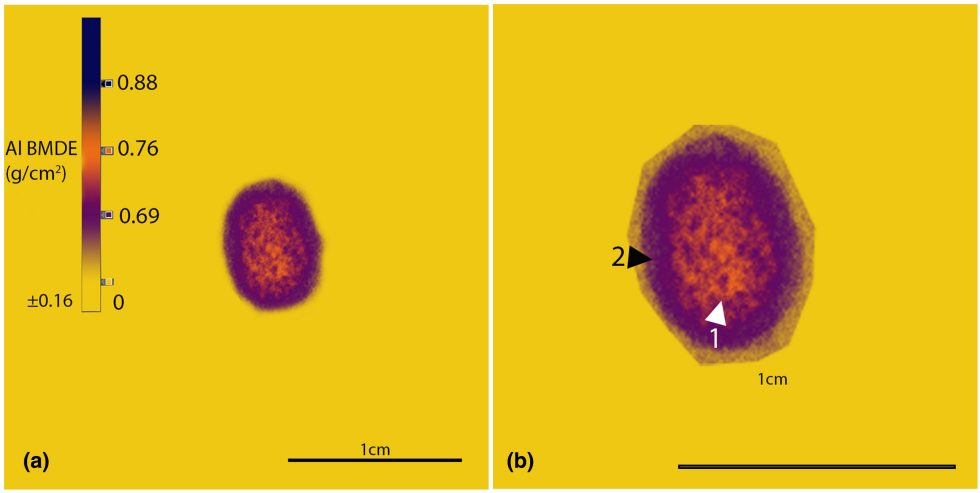

FIGURE 4 Annotated colour gradient map of a 38-week foetal Group 1 individual. Arrow descriptions are provided in Table 3.

TABLE 3 Radiographic features of a Group 1 talus. Arrows pertain to Figure 4.

Arrow	Feature
1	Radiopaque centre of talus associated with medium Al BMDE, depicted by orange.
2	Periphery of talus with greater radiolucency than the centre of the talus with lower Al BMDE depicted by violet.

linear trajectories from the body extending through the dorsal half of the talar head and neck (Figure 7, arrows 4 and 5). Overall, this specimen appeared to have a reduced radiodensity in comparison to Group 2 specimens due to the visible yellow background through the bone, and therefore Al BMDE. However, it is unclear whether this is due to a decrease in bone mineral density or due to the post-mortem damage to the bone, which interrupts both the cortical and trabecular structures (Figures 3 and 4).

3.4 | Group 4 (2–8 years)

Within Group 4, the 12 tali from 8 individuals appeared easily recognisable in comparison to previous groups, with a distinct body, neck, and head (Figures 3 and 4). Radiographically, the body of the talus appeared to be comprised of medium to high Al BMDE, with the lateral aspect of the trochlea exhibiting increased Al BMDE as maturity increased within this group (Figure 8, arrows 1 and 2). A consistent trajectory extending antero-laterally from the medial aspect of the talar body to the lateral talar head was observed (Figure 8, arrow 3). Viewed laterally, the pattern extending from the body, through the neck, and into the head appeared to be present within the superior half of the neck and head of the talus (Figure 8, arrows 4–8). Meanwhile, the body of the talus exhibited a pattern of rays extending vertically throughout this region of the bone (Figure 8, arrows 4 and 5).

3.5 | Group 5 (5–9 years)

In comparison to specimens within Group 4, the lateral process of the talus was more developed in the Group 5 stage (Figures 3 and 4). Specimens within Group 5 demonstrated the development of the radiographic patterns observed in Group 4; however, the area of high Al BMDE within the lateral trochlea increased in prominence, with a pattern appearing to extend out of this area and curve from the lateral aspect of the talus and into the midline (Figure 9, arrows 1), extending anteriorly into the neck (Figure 9, arrow 4). Medially, struts appeared to extend from the body and anterolaterally through the neck and into the head, as exhibited in Group 4 (Figure 9, arrows 2, 3, and 5). The lateral view of the talus also demonstrated a more developed version of the pattern observed within Group 4, with a trajectory evident running supero-inferiorly within the talar body (Figure 9, arrows 6–8). A pattern was also observed originating from the body and extending anteriorly into the neck and head in linear rays, which were more prominent in the superior half of the talus (Figure 9, arrows 9–11).

3.6 | Group 6 (9–14 years)

Group 6 tali, which consisted of 13 specimens from 7 individuals, demonstrated a morphology consistent with the adult talus, with a well-developed lateral process and lateral tubercle of the posterior process. In comparison to Group 5 specimens, the neck of the talus appeared elongated (Figures 3 and 8). Similar radiographic patterns were observed within Group 5, but they appeared more refined in Group 6 (Figures 3 and 8). The lateral trochlea demonstrated an area of high Al BMDE (Figure 10, arrow 1). A trajectory curved antero-medially from the lateral trochlea into the neck and head, while struts also extended linearly from the medial aspect of the body and into the neck (Figure 10, arrows 2 and 3). This then appeared to extend antero-laterally into the head of the talus and increase in Al

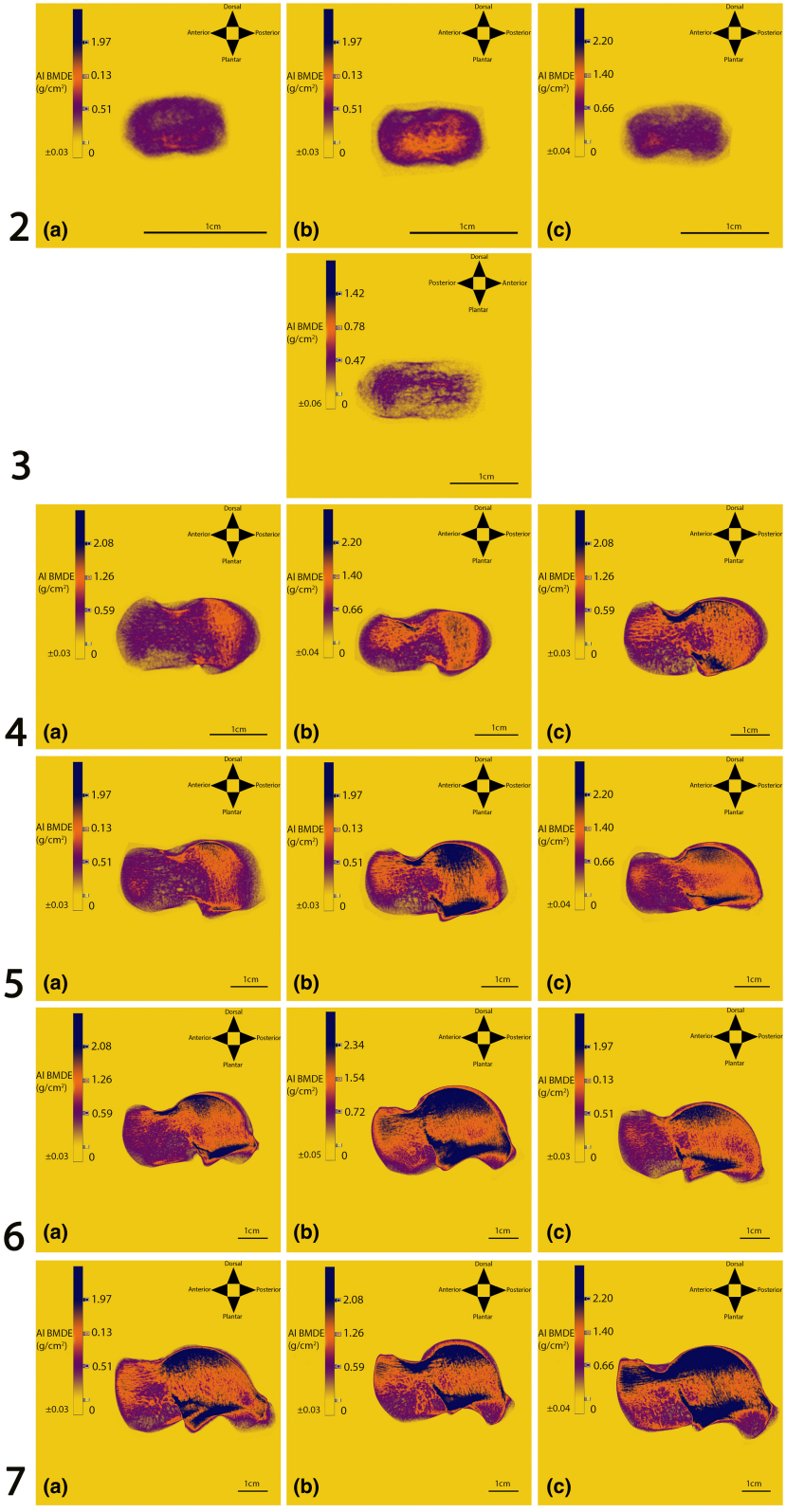

FIGURE 5 Lateral view of the developing talus. Group assignment on the left side of the figure. (a) Least developed; (b) median development; (c) most developed specimen within each developmental group. AI BMDE scale in each image.

BMDE in the distal direction (Figure 10, arrows 4 and 5). From the lateral view, the talus appeared similar to Group 5, but with a pattern of high AI BMDE extending through the superior aspect of the neck and throughout the head of the talus (Figure 10, arrow 11). Rays were also observed extending superiorly from the plantar surface of the head and neck (Figure 10, arrows 9 and 10).

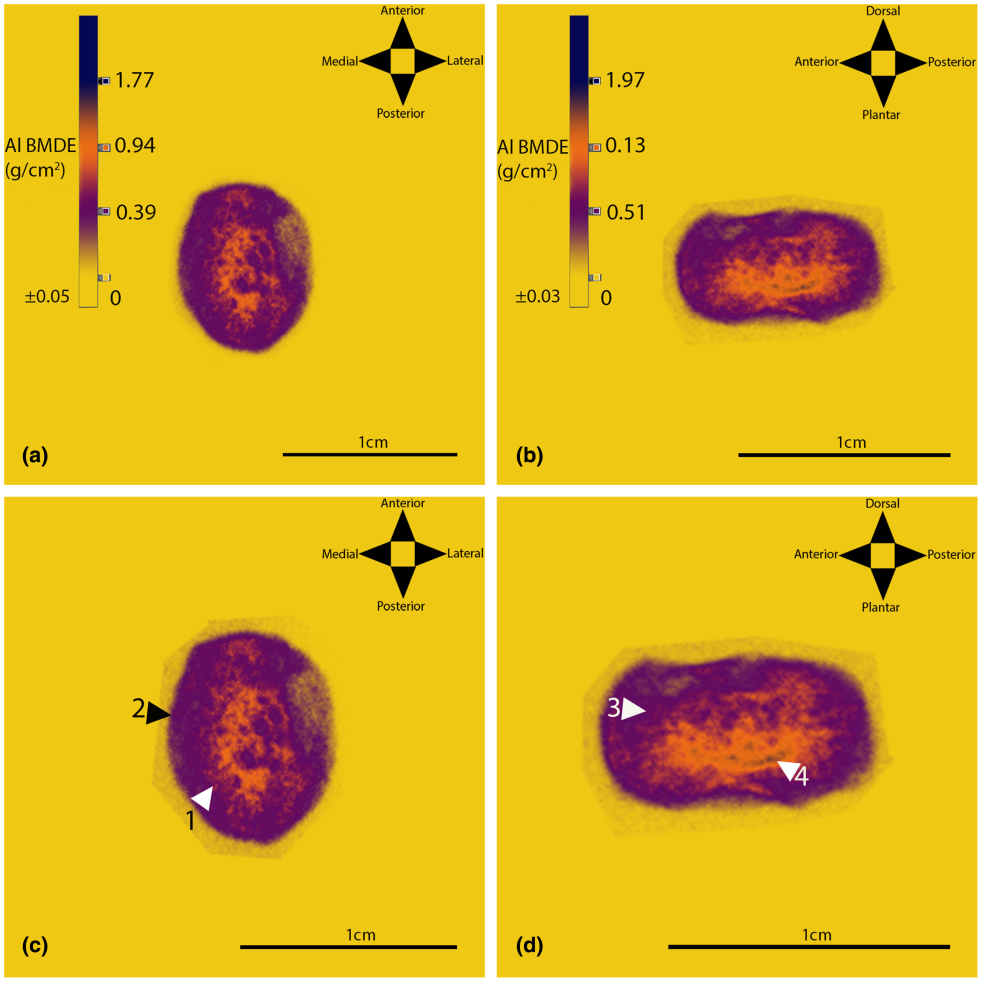

FIGURE 6 Annotated colour gradient map of a perinatal Group 2 individual. Arrow descriptions are provided in Table 4.

TABLE 4 Radiographic features of a Group 2 talus. Arrows pertain to Figure 6.

Arrow	Feature
1	C-shaped radiodensity within the centre of the talus with medium AI BMDE illustrated by orange.
2	Periphery of talus with lower AI BMDE than the centre demonstrated by the violet colour.
3	Medium AI BMDE within the centre of the talus which appears to decrease in prevalence from the plantar to the dorsal surface of the talus.
4	Small area superior to the sinus tali with high AI BMDE illustrated by a line of blue.

3.7 | Group 7 (16–20 years)

Radiographic patterns observed between Groups 6 and 7 were very similar, and as such, both groups overlap in age range (Figures 2, 3, and 5). However, these groups were distinguished radiographically by the prominent pattern of high AI BMDE, demarcated by blue, running antero-laterally from the medial aspect of the medial talar body and into the head of the talus via the neck observed within Group 7 specimens (Figure 11, arrows 3 and 4).

4 | DISCUSSION

The developing talus demonstrated distinct ontogenetic phases. The development of the talus can therefore be subdivided into foetal, perinatal, and refinement (>2 years). This is consistent with the progression of development described within the talus (Figus, Stephens, Sorrentino, Bortolini, Arrighi, Higgins, et al., 2022; Figus, Stephens, Sorrentino, Bortolini, Arrighi, Lugli, et al., 2022) and other regions of the skeleton (Acquaah et al., 2015; Beresheim et al., 2020; Colombo et al., 2019; Gosman & Ketcham, 2009; Maclean, 2017; Milovanovic et al., 2017; O'Malley, 2013; Reid et al., 2023; Ryan et al., 2017; Ryan & Krovitz, 2006; Saers et al., 2019).

Radiographic analysis of the foetal talus was limited due to its small size. At 28 weeks, there was a lack of a shared pattern between specimens; however, by 38 weeks, the centre of the talus

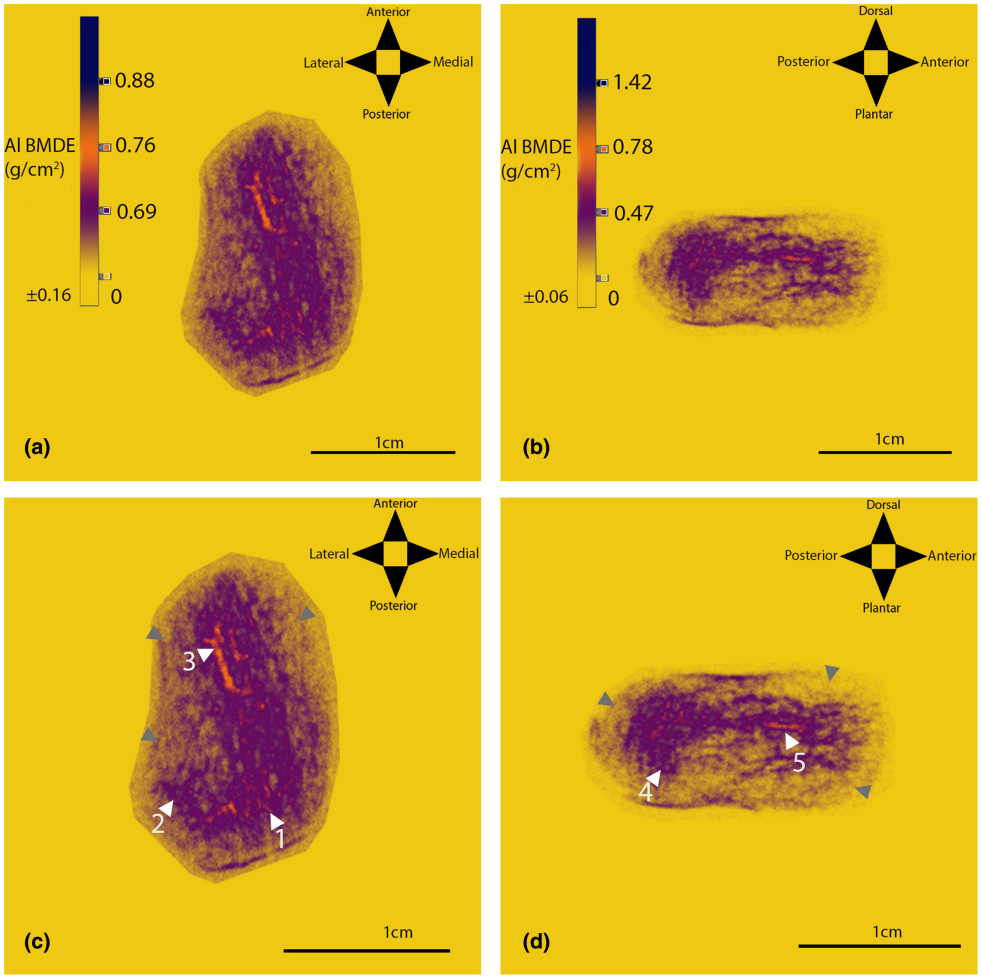

FIGURE 7 Annotated colour gradient map of a 1-year-old Group 3 individual. Arrow descriptions are provided in Table 5. Grey arrows indicate post-mortem damage.

TABLE 5 Radiographic features of a Group 3 talus. Arrows pertain to Figure 7.

Arrow	Feature
1	Medium Al BMDE illustrated by orange within the medial body.
2	Low Al BMDE demonstrated by the violet colour within lateral body.
3	Trajectory running from the medial body to the antero-lateral talar head.
4	Violet radiopaque area running superoinferiorly within the body.
5	Radiodense linear trajectories extending from the body through the dorsal half of the talar head and neck.

appeared more radiodense than the periphery of the bone. This appears consistent with previously reported ossification patterns of the talus, which progress from deep to superficial (Fritsch et al., 1996). This pattern was also observed radiographically in the foetal and perinatal lumbar vertebral centra (Goodchild, 2019; Nuzzo et al., 2003).

By the perinatal period, the talus had developed considerably in comparison to 28 weeks intrauterine. At this stage, an area of increased radiodensity was observed superior to the region of the sinus tarsi. This radiodense area is consistent with the location of the primary ossification centre of the talus, which has previously been described as originating in the neck region of the bone (Agrawal et al., 1984; Cheng et al., 1997; Fritsch et al., 1996; Hubbard et al., 1993). Thus, this area of elevated Al BMDE in comparison to the remainder of the perinatal talus may be attributed to its location as the primary ossification centre. Ossification of the talus continues from this area, purportedly expanding distally, proximally, and medially (Hubbard et al., 1993). Therefore, these areas are likely to be associated with lower Al BMDE in comparison to the primary ossification centre.

From the inferior radiographic view of 7 out of 10 perinatal tali specimens, a C-shaped radiodensity was observed in several specimens, with increased radiodensity towards the medial side (Figure 12). This indicates that there may be an organised pattern within the perinatal talus. Figus, Stephens, Sorrentino, Bortolini, Arrighi, Higgins, et al. (2022) did not conclude to have observed a pattern within the pre-loading juvenile talus following micro-computed

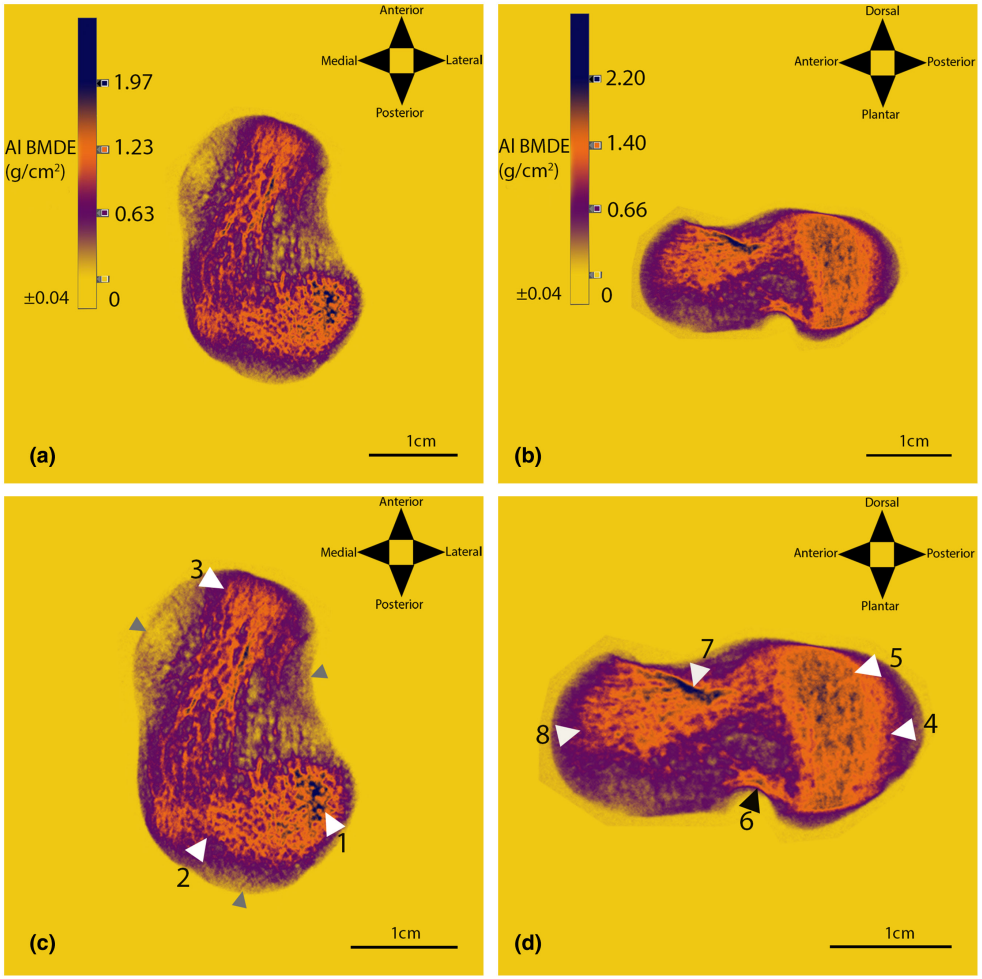

FIGURE 8 Annotated colour gradient map of a 6-year-old Group 4 individual. Arrow descriptions are contained within Table 6. Grey arrows indicate post-mortem damage.

TABLE 6 Radiographic features of a Group 4 talus. Arrows pertain to Figure 8.

Arrow	Feature
1	Area of high AI BMDE depicted by blue located within the lateral talar body.
2	The body of the talus predominately has medium values of AI BMDE than increases in prevalence from medial to lateral.
3	Trajectory of orange illustrating medium AI BMDE running anterolaterally between the body of the talus and the head, through the neck.
4	Area of medium AI BMDE illustrated by orange present throughout the body of the talus.
5	Trajectory of high AI BMDE depicted by blue extending superior-inferiorly through the body of the talus.
6	Area of medium to high AI BMDE with an orange and blue curvature along the trajectory of the sinus tali.
7	High AI BMDE observed within the superior neck of the talus. Blue struts extend anteriorly from this area into the head.
8	Prevalence of orange extending anteriorly within the superior half of the head of the talus.

tomography analysis; however, the patterns observed radiographically may not be reflected in BV/TV and DA values. Given that DA reflects the trabecular alignment, we would not expect to see this radiodensity reflected in the DA values unless there were clearly organised struts visible within the radiographs, such as the consistent trajectory extending antero-laterally from the medial aspect of the talar body to the lateral talar head in specimens from Group 4 onwards (Figure 7, arrow 3). This level of organisation does not appear to be present in the perinatal specimens. However, it could be hypothesised that a high radiodensity results in a high BV/TV result since BV/TV is the ratio of bone to the total volume analysed. Within Figus, Stephens, Sorrentino, Bortolini, Arrighi, Higgins, et al. (2022) morphometric maps of BV/TV means, the pre-loading group does appear to have increased BV/TV within the medial side of the talus

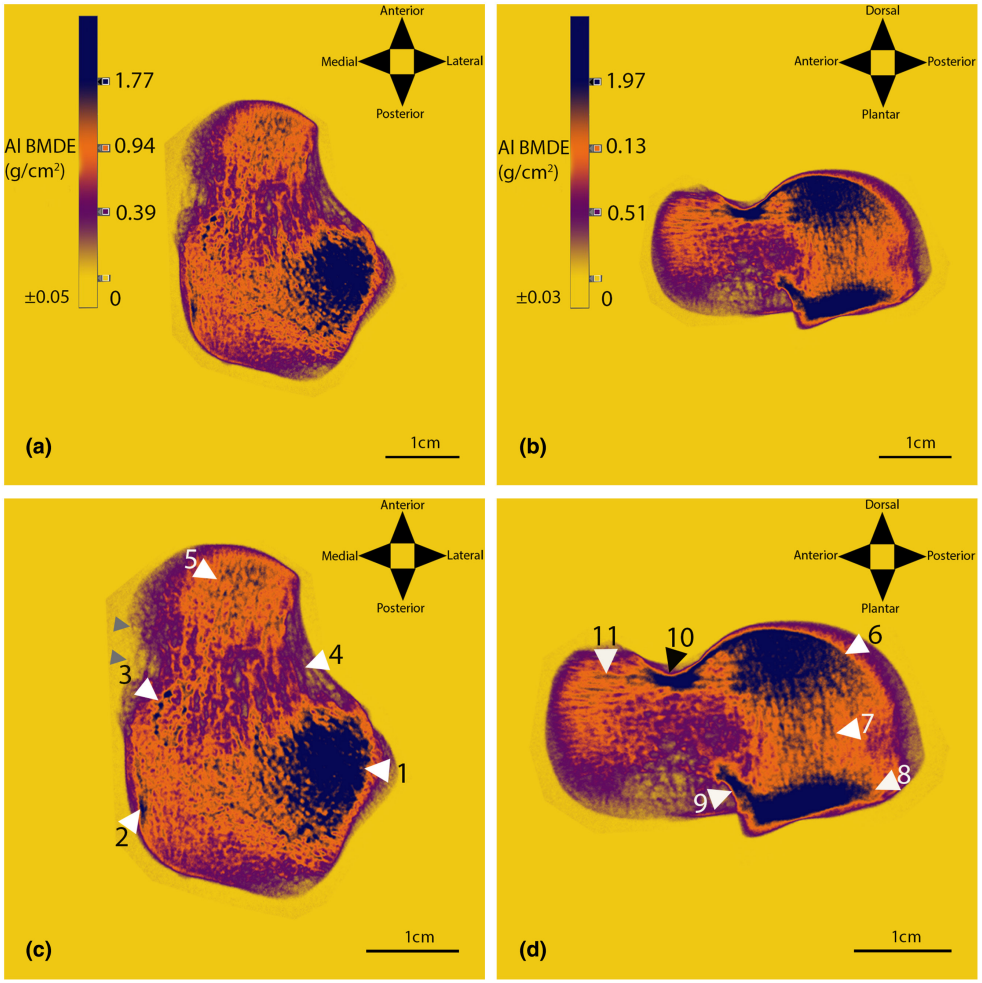

FIGURE 9 Annotated colour gradient map of an 8-year-old Group 5 individual. Arrow descriptions are provided in Table 7. Grey arrows indicate post-mortem damage.

TABLE 7 Radiographic features of a Group 5 talus. Arrows pertain to Figure 9.

Arrow	Feature
1	High Al BMDE depicted by blue within the lateral body of the talus.
2	Postero-medially within the body of the talus, linear orange struts appear to fan out from the posteromedial margin of the bone.
3	Trajectory of medium/high Al BMDE which extend from the medial aspect of the body of the talus and anterolaterally through the neck and into the head.
4	Striations which appear violet and orange that extend anteriorly from the lateral aspect of the talar body, through the neck and into the head.
5	Network of blue present within the head of the talus indicating high aluminium bone mineral density equivalents.
6	Semi-circle area of Al BMDE depicted by blue fanning from the superior body of the talus.
7	Trajectory of blue extending between the dorsal and plantar surface of the talar body.
8	Rectangular area of Al BMDE depicted by blue extending from the inferior body of the talus.
9	Area of high Al BMDE extending superiorly from the plantar anterior surface of the body in the region of the sinus tali/lateral process.
10	Blue area of high Al BMDE equivalents extending through the superior neck of the talus which is a continuation of the area demarcated by Arrow 6.
11	Linear trajectory travelling anteriorly through the head of the talus which range from medium to high Al BMDE, illustrated by blue and orange. Inferiorly within this area, these struts appear more mesh-like than linear.

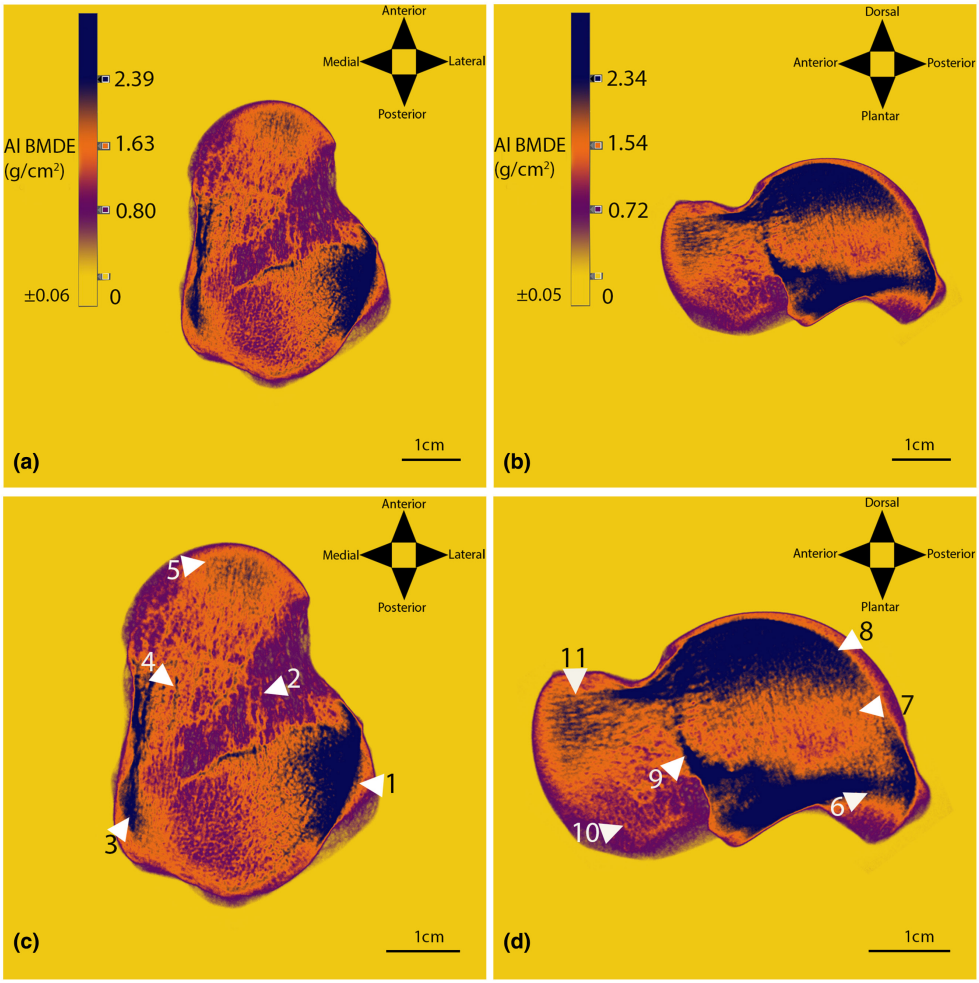

FIGURE 10 Annotated colour gradient map of a Group 6 individual estimated at 9–12 years of age at death. Arrow descriptions are provided in Table 8.

TABLE 8 Radiographic features of a Group 6 talus. Arrows pertain to Figure 10.

Arrow	Feature
1	High AI BMDE depicted by blue within the lateral body of the talus.
2	Orange struts within the central region of the neck of the talus.
3	Medial margin of the talus exhibits a line of blue depicting high AI BMDE.
4	Trajectory ranging from orange to blue extending anterolaterally through the neck of the talus from the medial aspect of the talus and into the head.
5	Blue network within the head of the talus.
6	Area of AI BMDE within the plantar aspect of the body which increases in prevalence from posterior to anterior.
7	Trajectory ranging from orange to blue present between the dorsal and plantar aspects of the talar body.
8	Semi-circular area of high AI BMDE within the superior aspect of the talar body.
9	Area of high AI BMDE extending superiorly from the sinus tali/lateral process.
10	Network of orange throughout the inferior portion of the head and neck of the talus extending superiorly and slightly anteriorly.
11	Blue trajectory within the dorsal half of the head of the talus which continue from Arrow 8 and indicate high AI BMDE.

in comparison to the remainder of the bone, which is consistent with the radiographic patterns observed here. This c-shaped radiodensity is not dissimilar to the radiodensity observed in the mature talus, with struts extending anteromedially from the lateral body of the talus and into the head, combined with the radiodensity within the body, which as a whole appears c-shaped. It could be that the c-shape radiodensity is a pre-existing scaffold on which the mature structure is developed.

Rudimentary patterns consistent with adult form have also been identified in the foetal ilium (Abel & Macho, 2011; Cunningham &

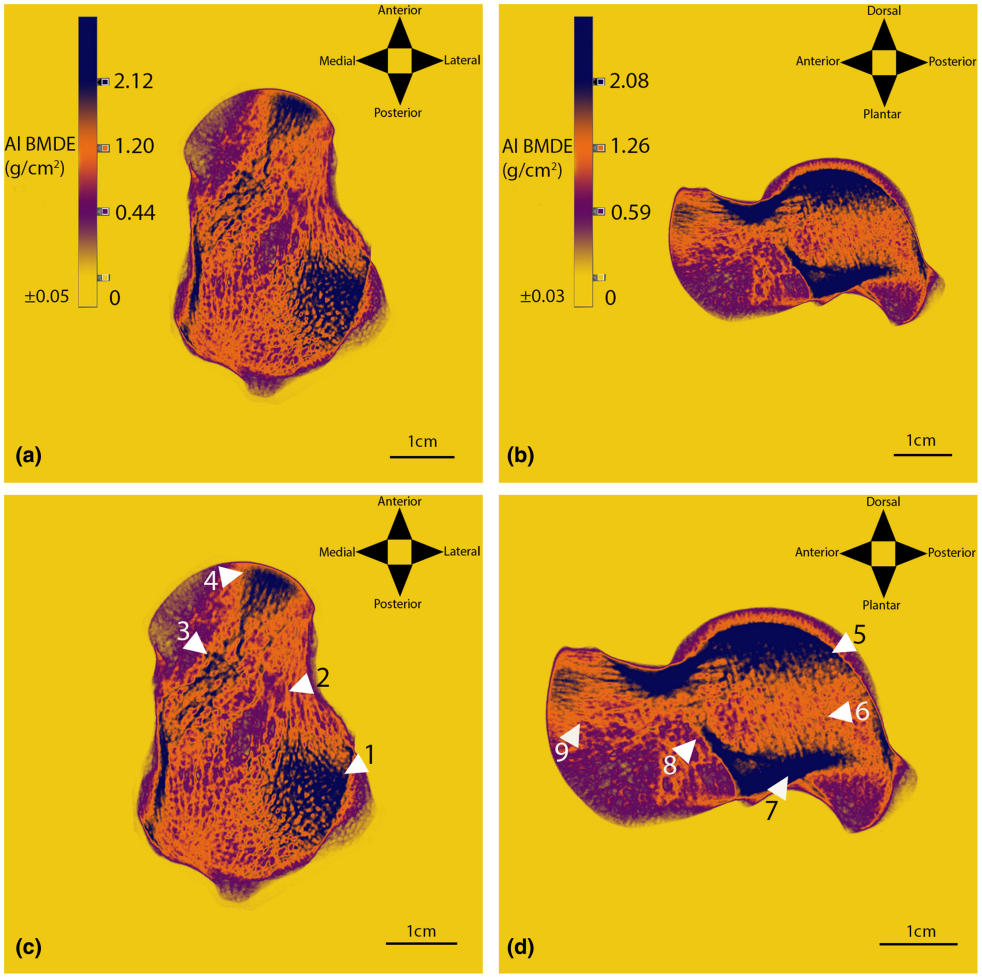

FIGURE 11 Annotated colour gradient map of a Group 7 individual estimated at 16–20 years of age at death. Arrow descriptions are provided in Table 9.

TABLE 9 Radiographic features of a Group 7 talus. Arrows pertain to Figure 11.

Arrow	Feature
1	High AI BMDE depicted by blue within the lateral body of the talus.
2	Orange struts extending anteromedially from the lateral body of the talus and into the head.
3	Trajectory of high AI BMDE depicted by blue extending anteromedially through neck of the talus and into the head.
4	The blue struts demarcated by Arrow 3 converge at the distal head of the talus in an area of dense blue.
5	Blue area of high AI BMDE within the dorsal aspect of the talar body.
6	Network of struts ranging from orange to blue present between the dorsal and plantar aspects of the talar body.
7	Area of high AI BMDE within the plantar aspect of the body.
8	Area of high AI BMDE extending superiorly from the sinus tali/lateral process.
9	Network of blue struts within the dorsal half of the head of the talus which continue from the body and indicate high AI BMDE.

Black, 2009a, 2009b), the sacrum (Yusof, 2013), and the scapula (O'Malley, 2013). These basic frameworks are suggested to be genetically predetermined and that bipedal forces are subsequently superimposed upon them.

Alternatively, the rudimentary pattern within the perinatal talus may be a result of the vascularisation pattern of the talus. Numerous vascular foramina can be observed macroscopically within the neck of the talus. These foramina coincide with areas of reduced AI BMDE in comparison to the rest of the bone, suggesting that the invasion of vessels influences the radiopacity of the talus. The cartilaginous anlage of the talus is the first tarsal to experience vascular invasion (Cheng et al., 1997; Fritsch et al., 1996), with cartilage canals appearing between 9 and 12 weeks (Agrawal et al., 1984; Gardner et al., 1959). By the perinatal period, the talus is supplied by vessels via branches from the sinus tarsi, deltoid, and superior neck vessels (Fritsch et al., 1996). Therefore, the

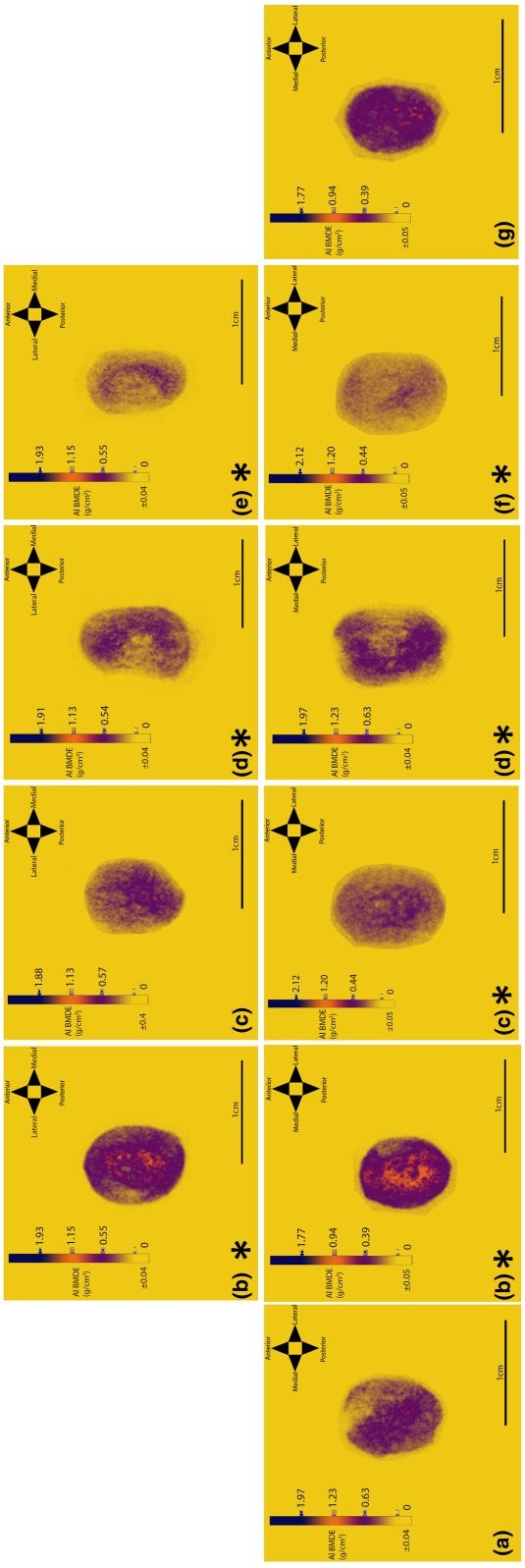

FIGURE 12 Colour maps of perinatal specimens. Specimens B–D are paired with the left talus on the upper row and the right on the lower row. Specimens with an asterisk are those in which a C-shaped radiodensity is present on the medial side.

organisation within the perinatal talus that appears as a template for the adult talus may be a result of the vascularisation pattern of the bone (Figure 1), rather than acting as a pre-determined template for locomotive forces to act upon. This neck area of the talus is also typically smaller in dimension than the rest of the bone, and therefore presents less tissue for x-rays to pass through and will appear more radiolucent than the rest of the bone. However, this radiolucency also appears from the lateral view, suggesting it is not solely related to differences in tissue thickness.

Additionally, these patterns coincide with the location of the calcaneal facets of the talus, which may contribute to this radiodensity. These general areas of increased radiodensity within the talus that can be observed in individuals older than 3 years of age may be associated with the developing subtalar facets (Figure 13).

The radiodense areas, outlined in white in Figure 13, coincide with the subtalar facets, allowing for the demarcation of these articular surfaces after 3 years of age. This may be attributed to weight-bearing due to the bipedal gait. This also coincides with the increase in BV/TV observed in the posterior subtalar facet between 3.1 and 6 years (Figus, Stephens, Sorrentino, Bortolini, Arrighi, Lugli, et al., 2022), which indicates that areas of articulation may experience increased BV/TV with the application of bipedal forces in comparison to non-articular areas. Morphological transformations of the talar facets after 8 years of age have been demonstrated to be strongly correlated with increasing bodyweight (Hellier & Jeffery, 2006). Thus, the prominent pattern of high Al BMDE, demarcated by blue, running antero-laterally from the medial aspect of the talar body and into the head of the talus via the neck observed within Group 7 specimens may be related to an increase in bodyweight following the pubertal growth spurt. A combination of the presence of the subtalar facets and the vascularisation of the talus may therefore contribute to the shared patterns identified between young and late adolescent individuals. Further research on a larger sample of perinatal tali is required to assess whether this rudimentary pattern is a superficial resemblance or is more significant.

Due to the paucity of talar specimens ranging 0–2 years within this sample, limited conclusions can be made regarding the talus during this period. The single talus examined within this age group exhibited post-mortem damage, and thus no observations of changes in Al BMDE can be made. In several skeletal elements, this age range has demonstrated a period of regression associated with reduced radiodensity and trabecular bone volume fraction (Acquaah et al., 2015; Gosman & Ketcham, 2009; Milovanovic et al., 2017; Reid et al., 2023; Ryan et al., 2017; Ryan & Krovitz, 2006; Saers et al., 2019). Therefore, further examination of a larger sample of tali during this age period is recommended to investigate whether the talus also demonstrates a regressive period. Additionally, the absence of specimens of this age results in a lack of observation as to whether the development of the longitudinal arch of the foot and ankle plantarflexion during walking around 18 months of age influences the internal structure of the developing talus.

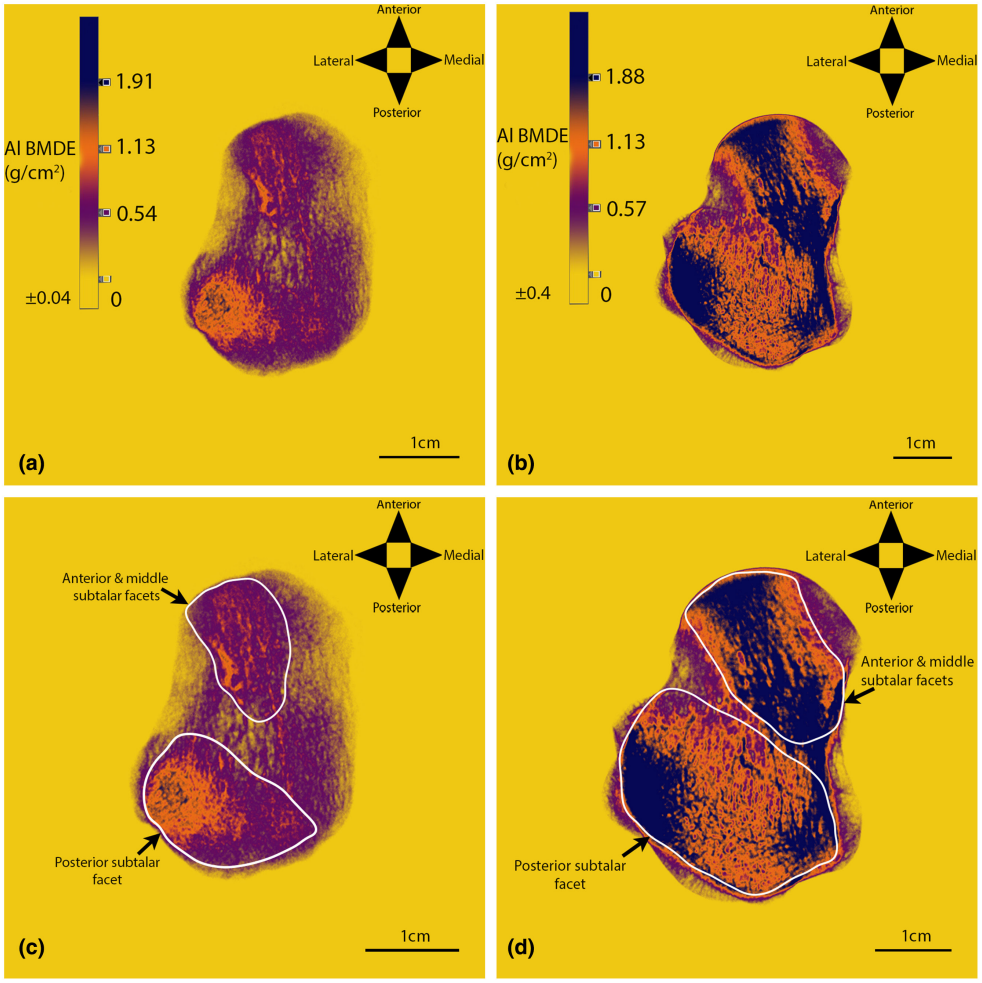

FIGURE 13 Development of subtalar facets in the left talus. (a) 4 years; (b) late adolescence. Top row is an unaltered image of the lower row. White outlines demarcate subtalar facets.

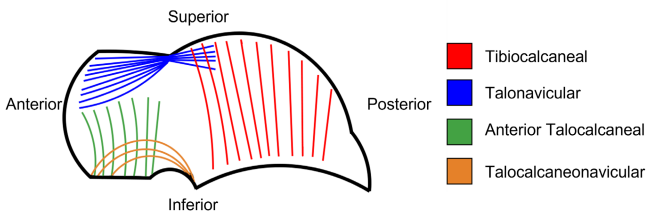

FIGURE 14 Proposed trajectories within the talus. Lateral view.

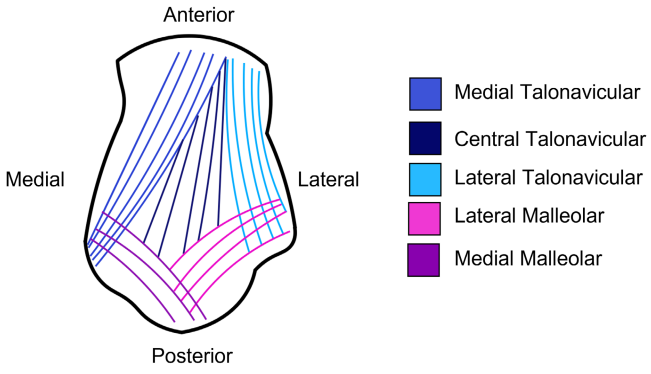

FIGURE 15 Proposed trajectories within the talus. Superior view.

While several trabecular trajectories are described within the literature examining the adult talus, they lack a standardised terminology. Therefore, based on the observations made in this study of the late adolescent (Group 7) talus combined with the adult literature, the following trajectories are proposed: tibiocalcaneal, medial malleolar, lateral malleolar, talonavicular (medial, central, and lateral), anterior talocalcaneal, and talocalcaneonavicular trajectories (Figures 14 and 15). The naming convention adopted is based on positional information. These are also simplifications of the trajectories of the radiographic patterns observed within the talus and identify the most evident trajectories.

A radiographic pattern was observed within the body of the adolescent tali that was orientated in more than one direction, identified as the medial and lateral malleolar trajectories (Figure 15). This pattern was identifiable in Group 3 specimens (from 1 year of age) and became more distinct with maturity. In the midline of the juvenile talar body, a sagittal trajectory was observed, named the central talonavicular trajectory (Figure 15). In the medial aspect of the juvenile talar body, a trajectory appears to radiate both anteriorly and posteriorly (medial talonavicular and medial malleolar trajectory, Figure 15). From the lateral view, a trajectory was observed

running supero-inferiorly within the body (tibiocalcaneal trajectory, Figure 14).

The adult body of the talus has been described as parallel trabecular plates running in the sagittal plane within the body (Ebraheim et al., 1999; Pal & Routal, 1998), while the talar body trabeculae were found to be orientated in two directions (Athavale et al., 2008; Takechi et al., 1982). The observations within the juvenile talus of the malleolar, talonavicular, and tibiocalcaneal trajectories within this study therefore agree with the latter description (Athavale et al., 2008; Takechi et al., 1982). Su et al. (2013) also described the trabeculae in the posterolateral trochlea as orientated slightly posteriorly towards the calcaneus, consistent with the lateral malleolar trajectory. The organisation within the body of the adult talus is believed to facilitate the transmission of forces from the body via the tibia and through the talus, both anteriorly towards the metatarsals and postero-inferiorly towards the calcaneus (Takechi et al., 1982). Therefore, this suggests the patterns observed within the developing juvenile talus are consistent with the trajectories observed within the adult talus. These adult trajectories have been strongly associated with the transmission of forces during walking (Pal & Routal, 1998; Takechi et al., 1982), and therefore their appearance may be attributed to the development of the bipedal gait in the juvenile talus. This is in agreement with the micro-computed tomography findings of Figus, Stephens, Sorrentino, Bortolini, Arrighi, Higgins, et al. (2022) and Figus, Stephens, Sorrentino, Bortolini, Arrighi, Lugli, et al. (2022) in the juvenile talus.

Additionally, the lateral body demonstrated an increasing area of high bone mineral density equivalents, demarcated by blue, as development progressed after 2 years of age. The lateral portion of the trochlea has been reported as an area of high BV/TV within adults (Saers et al., 2018; Tsegai et al., 2017), while the lateral side of the body has also demonstrated high BV/TV values (Figus, Stephens, Sorrentino, Bortolini, Arrighi, Lugli, et al., 2022). This appears to be correlated to the distribution of contact pressure during the adult gait cycle modelled by Bae et al. (2015) on the trochlear surface. They noted areas of high pressure occurring during the midstance and push-off phases of the gait cycle appearing on the antero-lateral quadrant of the talar surface, suggesting these areas are adapted to facilitate high pressures. Therefore, the increasing prevalence of blue, indicating high AI BMDE, observed within this area from 2 years of age may be related to developing bipedal gait, with this area in particular experiencing increasing pressures.

The neck of the talus appeared increasingly organised at 1 year of age. A trajectory appeared to extend from the body, through the neck, and into the head of the talus (talonavicular trajectory; Figures 14 and 15). From the inferior view, this trajectory appeared to extend anteriorly from the medial aspect of the anterior body and extend antero-laterally towards the lateral portion of the distal talar head (medial talonavicular trajectory; Figure 14). From the centre of the anterior body of the talus, trabeculae appear to extend in the sagittal plane through the neck (central talonavicular; Figure 15), while from the lateral body of the talus, the trajectory appears to curve along the outline of the lateral neck of the talus (lateral talonavicular; Figure 15).

The organisation of the inferior half of the neck of the talus is less easily discerned than the superior neck. In specimens of Group 4 (2–8 years) and less mature specimens of Group 5 (5–9 years), an arched-shaped trajectory appears to curve from the anterior plantar body and into the posterior aspect of the plantar surface of the head (talocalcaneonavicular trajectory; Figure 14). Additionally, vertically aligned struts can be observed within this area (anterior talocalcaneal trajectory; Figure 14). However, within the more mature specimens of Group 5, this organisation of the inferior half of the neck of the talus becomes less visible due to the superimposition of the lateral process.

The configuration of the neck of the developing juvenile talus conflicts with several studies that describe the adult talar neck as a dense, irregular network of trabeculae (Ebraheim et al., 1999; Pal & Routal, 1998; Sinha, 1985; Takechi et al., 1982). However, the observations agree with Athavale et al. (2008), who described the talar neck as organised and a continuation of plates from the body of the talus. The organised appearance of the talar neck is consistent with the theory that trabecular trajectories in the adult talus transmit forces both anteriorly towards the navicular and inferiorly towards the calcaneus, in addition to receiving ground reaction forces via the calcaneus (Pal & Routal, 1998; Takechi et al., 1982), and further indicates that the identification of similar trajectories within the juvenile talus is related to these biomechanical forces.

The head of the juvenile talus demonstrated clear radiographic patterns. The medial talonavicular trajectory extends antero-laterally from the medial aspect of the talar body and into the lateral aspect of the head of the talus. In the more mature specimens of Group 6, this trajectory appeared blue within its most distal aspect, indicating high-AI BMDE. This area of elevated high AI BMDE equivalents is in the region of the articular surface of the navicular. This is consistent with the description of curved trabecular plates in the sagittal plane within the head of the adult talus (Athavale et al., 2008; Ebraheim et al., 1999; Krause et al., 2013; Pal & Routal, 1998; Saers et al., 2018; Sinha, 1985; Takechi et al., 1982). Additionally, high BV/TV values have been observed at the articular surface of the navicular in the adult talus (Tsegai et al., 2017) and the juvenile talus (Figus, Stephens, Sorrentino, Bortolini, Arrighi, Higgins, et al., 2022, Figus, Stephens, Sorrentino, Bortolini, Arrighi, Lugli, et al., 2022). This arrangement within the head of the talus is thought to facilitate the transmission of compressive forces to the metatarsals and pressures from the talonavicular joint while also being adapted to facilitate the transmission of forces inferiorly to the calcaneus (Pal & Routal, 1998; Takechi et al., 1982).

The organisation of the juvenile talus appears closely aligned with its functional requirements within the ankle joint to facilitate the transmission of forces during passive standing and the bipedal gait from the body. This consists of the transmission of forces from the body via the tibia and through the talus, which is organised to pass forces anteriorly through to the forefoot and inferiorly to the calcaneus. This organisation appeared from 1 year of age, becoming more distinct at 2 years of age, which coincides with the acquisition of the bipedal gait and becomes more refined during ontogeny. Within the mature tali of Group 5 (5–9 years) and all specimens of

Group 6 (9–14 years), the organisation of the talus appears consistent with the adult form.

A combination of radiographic absorptiometry and colour gradient maps was employed following Reid et al. (2023) to facilitate the observation of the internal arrangement of the talus from the foetal stage to late adolescence. However, radiographic absorptiometry does not overcome limitations experienced with tissue superimposition within radiography, and therefore any AI BMDE reported will be affected. As a result, AI BMDE was used more as a guide for interpretation than for definitive comparisons, and no extensive quantification or analysis of these values was conducted. Likewise, the superimposition of tissues meant that it was not possible to accurately differentiate between trabecular and cortical structures. Nevertheless, radiographic colour maps have been established to be a useful tool for ontogenetic analysis by radiographic results from Cunningham and Black (2009a) and Maclean et al. (2014) displaying consistent observations with subsequent microcomputed tomography results from Cunningham and Black (2009b) and Maclean (2017). Additionally, the intra-observer agreement results demonstrated very good agreement, indicating this is a reliable method. This is supported by the good to very good intra- and inter-observer agreement results within the tibia (Reid et al., 2023).

The limitations of the sample must be acknowledged. Given the predominately archaeological nature of the Scheuer collection, it is unknown whether these results are applicable to a modern sample. Additionally, the influence of pathology and cause-of-death on the radiographic observations is undetermined.

5 | CONCLUSION

This study combined radiographic absorptiometry with colour gradient maps to investigate the developing juvenile talus. Distinct ontogenetic phases were observed. The foetal talus demonstrated limited radiographic features, but appeared consistent with reported ossification patterns. The perinatal talus demonstrated a rudimentary pattern consistent with the structural organisation observed within the late adolescent (Group 7) talus. This shared pattern is hypothesised to be related to the vascular pattern of the talus. After 2 years of age, the talus demonstrated refinement, where radiographic trajectories progressively developed into patterns consistent with adult trabecular organisation, which are strongly linked to the forces associated with the bipedal gait. The development of such trajectories from approximately 2 years of age occurs around the onset of walking at approximately 12–14.5 months of age, suggesting a strong influence of locomotive forces on the development of the distal tibia and talus.

AUTHOR CONTRIBUTIONS

Rebecca A.G. Reid: study design, data acquisition and collection, data interpretation, manuscript design, preparation, revision, and review. Craig Cunningham: manuscript revision and review. Catriona Davies: manuscript revision and review.

ACKNOWLEDGMENTS

This work was supported by the University of Dundee Greenhouse Scholarship. Many thanks to Ms. Claire Cunningham and Mr. Tyler Halliwell for their technical radiographic assistance.

FUNDING INFORMATION

This work was supported by the University of Dundee Greenhouse Scholarship.

CONFLICT OF INTEREST STATEMENT

None.

DATA AVAILABILITY STATEMENT

Data available on request from authors. The data that support the findings of this study are available from the corresponding author upon reasonable request.

ORCID

Rebecca A. G. Reid https://orcid.org/0000-0002-1325-1963

REFERENCES

Abel, R. & Macho, G.A. (2011) Ontogenetic changes in the internal and external morphology of the ilium in modern humans. *Journal of Anatomy*, 218(3), 324–335.

Acquaah, F., Robson Brown, K.A., Ahmed, F., Jeffery, N. & Abel, R.L. (2015) Early trabecular development in human vertebrae: overproduction, constructive regression, and refinement. *Frontiers in Endocrinology*, 6, 67.

Adolph, K.E., Vereijken, B. & Denny, M.A. (1998) Learning to crawl. *Child Development*, 69(5), 1299–1312.

Adolph, K.E., Vereijken, B. & Shrout, P.E. (2003) What changes in infant walking and why. *Child Development*, 74(2), 475–497.

Agrawal, P., Atre, P.R. & Kulkarni, D.S. (1984) The role of cartilage canals in the ossification of the talus. *Acta Anatomica*, 119(4), 238–240.

Athavale, S.A., Joshi, S.D. & Joshi, S.S. (2008) Internal architecture of the talus. *Foot and Ankle International*, 29(1), 82–86.

Bae, J.Y., Park, K.S., Seon, J.K. & Jeon, I. (2015) Analysis of the effects of normal walking on ankle joint contact characteristics after acute inversion ankle sprain. *Annals of Biomedical Engineering*, 43(12), 3015–3024.

Baker, B.J., Tocheri, M.W. & Dupras, T.L. (2005) In: Baker, B.J., Tocheri, M.W. & Kulkarni, D.S. (Eds.) *The osteology of infants and children*, 1st edition. Texas: Texas A and M University Press.

Barak, M.M., Lieberman, D.E. & Hublin, J.-J. (2011) A Wolff in sheep's clothing: trabecular bone adaptation in response to changes in joint loading orientation. *Bone*, 49(6), 1141–1151.

Beresheim, A.C., Pfeiffer, S. & Grynpas, M. (2020) Ontogenetic changes to bone microstructure in an archaeologically derived sample of human ribs. *Journal of Anatomy*, 236(3), 448–462.

Bertsch, C., Unger, H., Winkelmann, W. & Rosenbaum, D. (2004) Evaluation of early walking patterns from plantar pressure distribution measurements. First year results of 42 children. *Gait and Posture*, 19(3), 235–242.

Bisi, M.C. & Stagni, R. (2015) Evaluation of toddler different strategies during the first six-months of independent walking: a longitudinal study. *Gait and Posture*, 41(2), 574–579.

Bosch, K., Gerss, J. & Rosenbaum, D. (2007) Preliminary normative values for foot loading parameters of the developing child. *Gait and Posture*, 26(2), 238–247.

Burrows, M., Liu, D., Moore, S. & McKay, H. (2010) Bone microstructure at the distal tibia provides a strength advantage to males in late

puberty: an HR-pQCT study. *Journal of Bone and Mineral Research*, 25(6), 1423–1432.

Chang, C.L., Kubo, M., Buzzi, U. & Ulrich, B. (2006) Early changes in muscle activation patterns of toddlers during walking. *Infant Behavior and Development*, 29(2), 175–188.

Cheng, X., Wang, Y., Qu, H. & Jiang, Y. (1995) Ossification processes and perichondral ossification groove of Ranvier: a morphological study in developing human calcaneus and talus. *Foot and Ankle International*, 16(1), 7–10.

Cheng, X., Wang, Y. & Qu, H. (1997) Intrachondral microvasculature in the human fetal talus. *Foot and Ankle International*, 18(6), 335–338.

Cicchetti, D.V. & Allison, T. (1971) A new procedure for assessing reliability of scoring EEG sleep recordings. *American Journal of EEG Technology*, 11, 101–109.

Colombo, A., Stephens, N.B., Tsegai, Z.J., Bettuzzi, M., Morigi, M.P., Belcastro, M.G. et al. (2019) Trabecular analysis of the distal radial metaphysis during the acquisition of crawling and bipedal walking in childhood: a preliminary study. *Bulletins et Mémoires de la Société d'Anthropologie de Paris*, 31(1–2), 43–51.

Cowgill, L.W., Warrener, A., Pontzer, H. & Ocobock, C. (2010) Waddling and toddling: the biomechanical effects of an immature gait. *American Journal of Physical Anthropology*, 143(1), 52–61.

Crock, H. (1996) Chapter 8–pelvic and lower limb bones. In: *An atlas of vascular anatomy of the skeleton and spinal cord*, 1st edition). (Figure 8.112a, pp.278). Oxfordshire: Taylor & Francis Ltd.

Cunningham, C., Scheuer, L. & Black, S. (2016) Chapter 12—the lower limb. In: Cunningham, C., Scheuer, L. & Black, S. (Eds.) *Developmental Juvenile Osteology*, 2nd edition. London: Academic Press, pp. 385–472.

Cunningham, C.A. & Black, S.M. (2009a) Development of the fetal ilium—challenging concepts of bipedality. *Journal of Anatomy*, 214(1), 91–99.

Cunningham, C.A. & Black, S.M. (2009b) Anticipating bipedalism: trabecular organization in the newborn ilium. *Journal of Anatomy*, 214(6), 817–829.

Cunningham, C.A. & Black, S.M. (2010) The neonatal ilium-Metaphyseal drivers and vascular passengers. *The Anatomical Record: Advances in Integrative Anatomy and Evolutionary Biology*, 293(8), 1297–1309.

Cunningham, C.A. & Black, S.M. (2013) The vascular collar of the ilium—Three-dimensional evaluation of the dominant nutrient foramen: the iliac nutrient collar. *Clinical Anatomy*, 26(4), 502–508.

Currey, J. (1984) *The mechanical adaptations of bones*. New Jersey: Princeton University Press.

Czerwiński, F., Tomasik, E. & Mahaczek-Kodowska, A. (2001) The ossification of tarsal bones and distal end of the tibia in human foetus. *Folia Morphologica*, 60(3), 195–198.

de Vries, J.I.P., Visser, G.H.A. & Prechtl, H.F.R. (1982) The emergence of fetal behaviour. I. Qualitative aspects. *Early Human Development*, 7(4), 301–322.

Ding, M., Danielsen, C.C., Hvid, I. & Overgaard, S. (2012) Three-dimensional microarchitecture of adolescent cancellous bone. *Bone*, 51(5), 953–960.

Djuric, M., Milovanovic, P., Djonic, D., Minic, A. & Hahn, M. (2012) Morphological characteristics of the developing proximal femur: a biomechanical perspective. *Srpski Arhiv Za Celokupno Lekarstvo*, 140(11–12), 738–745.

Ebraheim, N.A., Sabry, F.F. & Nadim, Y. (1999) Internal architecture of the talus: implication for Talar fracture. *Foot and Ankle International*, 20(12), 794–796.

Figus, C., Stephens, N.B., Sorrentino, R., Bortolini, E., Arrighi, S., Higgins, O.A. et al. (2022) Morphologies in-between: the impact of the first steps on the human talus. *The Anatomical Record*, 306(1), 124–142.

Figus, C., Stephens, N.B., Sorrentino, R., Bortolini, E., Arrighi, S., Lugli, F. et al. (2022) Human talar ontogeny: insights from morphological and trabecular changes during postnatal growth. *American Journal of Biological Anthropology*, 179(2), 211–228.

Fritsch, H., Schmitt, O. & Eggers, R. (1996) The ossification Centre of the talus. *Annals of Anatomy-Anatomischer Anzeiger*, 178(5), 455–459.

Frost, H.M. (2003) Bone's mechanostat: a 2003 update. *The Anatomical Record Part A: Discoveries in Molecular, Cellular, and Evolutionary Biology*, 275A(2), 1081–1101.

Gardner, E., Gray, D.J. & O'Rahilly, R. (1959) The prenatal development of the skeleton and joints of the human foot. *The Journal of Bone and Joint Surgery American*, 41-A(5), 847–876.

Gefen, A., Megido-Ravid, M., Itzchak, Y. & Arcan, M. (2000) Biomechanical analysis of the three-dimensional foot structure during gait: A basic tool for clinical applications. *Journal of Biomechanical Engineering*, 122(6), 630–639.

Glorieux, F.H., Travers, R., Taylor, A., Bowen, J.R., Rauch, F., Norman, M. et al. (2000) Normative data for iliac bone histomorphometry in growing children. *Bone*, 26(2), 103–109.

Goliath, J.R., Gosman, J., Stout, S. & Ryan, T. (2022) Ontogenetic patterning of human subchondral bone microarchitecture in the proximal tibia. *Biology*, 11(7), 1002.

Goodchild, S. (2019) *A qualitative and quantitative analysis of the developing lumbar vertebral column*. PhD Thesis. Dundee: University of Dundee. https://discovery.dundee.ac.uk/en/studentTheses/a-qualitative-and-quantitative-analysis-of-the-developinGg-human-l

Gosman, J.H. & Ketcham, R.A. (2009) Patterns in ontogeny of human trabecular bone from SunWatch Village in the prehistoric Ohio Valley: general features of microarchitectural change. *American Journal of Physical Anthropology*, 138(3), 318–332.

Hallemans, A., De Clercq, D., Otten, B. & Aerts, P. (2005) 3D joint dynamics of walking in toddlers: a cross-sectional study spanning the first rapid development phase of walking. *Gait and Posture*, 22(2), 107–118.

Hallemans, A., D'Août, K., De Clercq, D. & Aerts, P. (2003) Pressure distribution patterns under the feet of new walkers: The first two months of independent walking. *Foot & Ankle International*, 24(5), 444–453. Available from: https://doi.org/10.1177/107110070302400513

Hébert, D., Lebrun, R. & Marivaux, L. (2012) Comparative three-dimensional structure of the trabecular bone in the talus of primates and its relationship to ankle joint loads generated during locomotion. *The Anatomical Record*, 295(12), 2069–2088.

Hellier, C.A. & Jeffery, N. (2006) Morphological plasticity in the juvenile talus. *Foot and Ankle Surgery*, 12(3), 139–147.

Hubbard, A.M., Meyer, J.S., Davidson, R.S., Mahboubi, S. & Harty, M.P. (1993) Relationship between the ossification center and cartilaginous anlage in the normal hindfoot in children: study with MR imaging. *American Journal of Roentgenology*, 161(4), 849–853.

Johnston, L., Eastwood, D. & Jacobs, B. (2014) Variations in normal gait development. *Paediatrics and Child Health*, 24(5), 204–207.

Keen, M. (1993) Early development and attainment of normal mature gait. *Journal of Prosthetics and Orthotics*, 5(2), 35–38.

Kneissel, M., Roschger, P., Steiner, W., Schamall, D., Kalchhauser, G., Boyde, A. et al. (1997) Cancellous bone structure in the growing and aging lumbar spine in a historic Nubian population. *Calcified Tissue International*, 61(2), 95–100.

Krause, M., Rupprecht, M., Mumme, M., Püschel, K., Amling, M. & Barvencik, F. (2013) Bone microarchitecture of the talus changes with aging. *Clinical Orthopaedics and Related Research*, 471(11), 3663–3671.

Landis, J.R. & Koch, G.G. (1977) The measurement of observer agreement for categorical data. *Biometrics*, 33(1), 159–174.

Maclean, S.J. (2017) *A qualitative and quantitative analysis of the juvenile ischium*. PhD Thesis. Dundee: University of Dundee. https://discovery.dundee.ac.uk/en/studentTheses/a-qualitative-and-quantitative-analysis-of-the-juvenile-ischium

Maclean, S.J., Black, S.M. & Cunningham, C.A. (2014) The developing juvenile ischium: macro-radiographic insights: the developing juvenile ischium. *Clinical Anatomy*, 27(6), 906–914.

Milovanovic, P., Djonic, D., Hahn, M., Amling, M., Busse, B. & Djuric, M. (2017) Region-dependent patterns of trabecular bone growth in the human proximal femur: a study of 3D bone microarchitecture from early postnatal to late childhood period. *American Journal of Physical Anthropology*, 164(2), 281–291.

Modlesky, C.M., Whitney, D.G., Carter, P.T., Allerton, B.M., Kirby, J.T. & Miller, F. (2014) The pattern of trabecular bone microarchitecture in the distal femur of typically developing children and its effect on processing of magnetic resonance images. *Bone*, 60, 1–7.

Nuzzo, S., Meneghini, C., Braillon, P., Bouvier, R., Mobilio, S. & Peyrin, F. (2003) Microarchitectural and physical changes during fetal growth in human vertebral bone. *Journal of Bone and Mineral Research*, 18(4), 760–768.

Okamoto, T., Okamoto, K. & Andrew, P.D. (2003) Electromyographic developmental changes in one individual from newborn stepping to mature walking. *Gait and Posture*, 17(1), 18–27.

O'Malley, A. (2013) *A qualitative and quantitative investigation of the functional morphology of the juvenile scapula*. PhD Thesis. Dundee: University of Dundee. https://discovery.dundee.ac.uk/en/studentTheses/a-qualitative-and-quantitative-investigation-of-the-functional-mo

Osborne, D., Effmann, E., Broda, K. & Harrelson, J. (1980) The development of the upper end of the femur, with special reference to its internal architecture. *Radiology*, 137(1 Pt 1), 71–76.

Pal, G.P. & Routal, R.V. (1998) Architecture of the cancellous bone of the human talus. *The Anatomical Record*, 252(2), 185–193.

Perchalski, B., Placke, A., Sukhdeo, S.M., Shaw, C.N., Gosman, J.H., Raichlen, D.A. et al. (2018) Asymmetry in the cortical and trabecular bone of the human Humerus during development. *The Anatomical Record*, 301(6), 1012–1025.

Raichlen, D.A., Gordon, A.D., Foster, A.D., Webber, J.T., Sukhdeo, S.M., Scott, R.S. et al. (2015) An ontogenetic framework linking locomotion and trabecular bone architecture with applications for reconstructing hominin life history. *Journal of Human Evolution*, 81, 1–12.

Reid, R.A.G., Davies, C. & Cunningham, C. (2023) The developing juvenile distal tibia: radiographic identification of distinct ontogenetic phases and structural trajectories. *Journal of Anatomy*, 242(2), 191–212.

Reissis, D. & Abel, R.L. (2012) Development of fetal trabecular microarchitecture in the humerus and femur. *Journal of Anatomy*, 220(5), 496–503.

Roschger, P., Grabner, B.M., Rinnerthaler, S., Tesch, W., Kneissel, M., Berzlanovich, A. et al. (2001) Structural development of the mineralized tissue in the human L4 vertebral body. *Journal of Structural Biology*, 136(2), 126–136.

Rose, J. & Gamble, J.G. (1994) In: Rose, J. & Gamble, J.G. (Eds.) *Human Walking*, 2nd edition. Baltimore: Lippincott Williams and Wilkins.

Ruff, C., Holt, B. & Trinkaus, E. (2006) Who's afraid of the big bad Wolff?: "Wolff's law" and bone functional adaptation. *American Journal of Physical Anthropology*, 129(4), 484–498.

Ruimerman, R., Hilbers, P., van Rietbergen, B. & Huiskes, R. (2005) A theoretical framework for strain-related trabecular bone maintenance and adaptation. *Journal of Biomechanics*, 38(4), 931–941.

Ryan, T.M. & Krovitz, G.E. (2006) Trabecular bone ontogeny in the human proximal femur. *Journal of Human Evolution*, 51(6), 591–602.

Ryan, T.M., Raichlen, D.A. & Gosman, J.H. (2017) Structural and mechanical changes in trabecular bone during early development in the human femur and Humerus. In: Percival, C.J. & Richtsmeier, J.T. (Eds.) *Building bones: bone formation and development in anthropology*. Cambridge: Cambridge University Press, pp. 281–302.

Saers, J.P.P., Ryan, T.M. & Stock, J.T. (2018) Trabecular bone functional adaptation and sexual dimorphism in the human foot. *American Journal of Physical Anthropology*, 168(1), 154–169.

Saers, J.P.P., Ryan, T.M. & Stock, J.T. (2019) Baby steps towards linking calcaneal trabecular bone ontogeny and the development of bipedal human gait. *Journal of Anatomy*, 236(3), 474–492.

Saers, J.P.P., Gordon, A.D., Ryan, T.M. & Stock, J.T. (2022) Growth and development of trabecular structure in the calcaneus of Japanese macaques (*Macaca fuscata*) reflects locomotor behavior, life history, and neuromuscular development. *Journal of Anatomy*, 241(1), 67–81.

Salle, B.L., Rauch, F., Travers, R., Bouvier, R. & Glorieux, F.H. (2002) Human fetal bone development: Histomorphometric evaluation of the proximal femoral metaphysis. *Bone*, 30(6), 823–828.

Sinha, D.N. (1985) Cancellous structure of tarsal bones. *Journal of Anatomy*, 140(Pt 1), 111–117.

Soames, R.W. & Palastanga, N. (2019) Lower Limb. In: Soames, R.W. & Palastanga, N. (Eds.) *Anatomy and human movement*, 7th edition. London: Elsevier, pp. 219–434.

Størvold, G.V., Aarethun, K. & Bratberg, G.H. (2013) Age for onset of walking and prewalking strategies. *Early Human Development*, 89(9), 655–659.

Su, A., Wallace, I.J. & Nakatsukasa, M. (2013) Trabecular bone anisotropy and orientation in an early Pleistocene hominin talus from East Turkana, Kenya. *Journal of Human Evolution*, 64(6), 667–677.

Sutherland, D. (1997) The development of mature gait. *Gait & Posture*, 6(2), 163–170.

Sutherland, D.H., Olshen, R.A., Biden, E.N. & Wyatt, M.P. (1988) In: Sutherland, D.H., Olshen, R.A., Biden, E.N. & Wyatt, M.P. (Eds.) *The development of mature walking*. London: Mac Keith Press.

Takechi, H., Ito, S., Takada, T. & Nakayama, H. (1982) Trabecular architecture of the ankle joint. *Anatomia Clinica*, 4(3), 227–233.

Tsegai, Z.J., Skinner, M.M., Gee, A.H., Pahr, D.H., Treece, G.M., Hublin, J.J. et al. (2017) Trabecular and cortical bone structure of the talus and distal tibia in pan and homo. *American Journal of Physical Anthropology*, 163(4), 784–805.

Verbruggen, S.W., Kainz, B., Shelmerdine, S.C., Hajnal, J.V., Rutherford, M.A., Arthurs, O.J. et al. (2018) Stresses and strains on the human fetal skeleton during development. *Journal of the Royal Society Interface*, 15(138), 20170593.

Yusof, N.A. (2013) *The development and anatomy of the sacrum in relation to the ilium and the sacroiliac joint*. PhD Thesis. Dundee: University of Dundee. https://discovery.dundee.ac.uk/en/studentTheses/the-development-and-anatomy-of-the-sacrum-in-relation-to-the-iliu

How to cite this article: Reid, R.A.G., Davies, C. & Cunningham, C. (2023) The developing juvenile talus: Radiographic identification of distinct ontogenetic phases and structural trajectories. *Journal of Anatomy*, 00, 1–21. Available from: https://doi.org/10.1111/joa.13940